From neural border to migratory stage: A comprehensive single cell roadmap of the timing and regulatory logic driving cranial and vagal neural crest emergence

Aleksandr Kotov[1,2], Mansour Alkobtawi[1,2]†, Subham Seal[1,2]†, Vincent Kappès[1,2], Sofia Medina Ruiz[3], Hugo Arbès[1,2], Richard Harland[3], Leonid Peshkin[4], and Anne H. Monsoro-Burq[1,2,5*]

Affiliations

[1]Université Paris Saclay, Faculté des Sciences d'Orsay, CNRS UMR 3347, INSERM U1021, rue Henri Becquerel, F-91405 Orsay, France.

[2]Institut Curie Research Division, PSL Research University, CNRS UMR 3347, INSERM U1021, Rue Henri Becquerel, F-91405 Orsay, France.

[3] Molecular and Cell Biology Department, Genetics, Genomics and Development Division, University of California Berkeley, CA 94720, USA.

[4]Systems Biology, Harvard Medical School, Boston, MA 02115, USA.

[5]Institut Universitaire de France, F-75005 Paris, France.

* corresponding author: anne-helene.monsoro-burq@curie.fr

Abstract

Neural crest cells exemplify cellular diversification from a multipotent progenitor population. However, the full sequence of molecular choices orchestrating the emergence of neural crest heterogeneity from the embryonic ectoderm remains elusive. Gene-regulatory-networks (GRN) govern early development and cell specification towards definitive neural crest. Here, we combine ultra-dense single cell transcriptomes with machine-learning and large-scale experimental validation to provide a comprehensive GRN underlying neural crest fate diversification from induction to early migration stages. During gastrulation, a transient neural border zone state precedes choice between neural crest and placodes following a "dual convergence model". Transcription factor connectome and bifurcation analyses demonstrate the early emergence of neural crest fates at neural plate stage, alongside an unbiased multipotent lineage persisting until after epithelial-mesenchymal transition. We decipher the circuits driving cranial and vagal neural crest formation and provide a broadly applicable strategy for investigating SC transcriptomes in vertebrate GRNs in development, evolution and disease.

Introduction

Neural crest cells form a population of multipotent and migratory progenitors found in vertebrate embryos, essential for the peripheral and enteric nervous system, craniofacial structures, endocrine and pigment cells among others. Together with ectodermal placodes, neural crest (NC) cells are evolutionary inventions that support many cell and tissue innovations promoting the vertebrate predatory lifestyle. Shortly after gastrulation, in the anterior-most part of the embryo, NC cells are induced from the dorsal-lateral "neural border zone" (NB), an ectoderm domain located between the non-neural ectoderm and the neural plate ectoderm (*1*, *2*). In addition to neural crest, NB territory also gives rise to posterior placodes, non-neural ectoderm and the dorsal part of the neural tube (*3*, *4*). Whether these four cell types arise from a common and multipotent early progenitor state, and how fate decisions are orchestrated at the NB during gastrulation remain poorly understood. During neurulation, NC specification and induction progresses as an anterior-to-posterior wave along the edges of the neural plate, with gene programs that define early and immature neural crest cells (e.g.

expression of *snail2, foxd3* and *sox8* genes) followed by later pre-migratory programs presaging emigration of NC cells from the NB epithelium as the neural folds elevate and close (e.g. expression of *sox10*, *twist1* and *cdh2 (N-cadherin)* genes; activation of specific metabolic and signaling pathways) (*5*, *6*). In addition to this pan-NC program, several regional molecular modules are activated along the anterior-posterior body axis and define sub-populations with specific potential (*7*, *8*). How these programs are interconnected with the pan-NC module, and how and when they are activated in pre-migratory NC cells is poorly described. Later, at the end of neurulation, NC cells leave the dorsal ectoderm by a stereotypical epithelium-to-mesenchymal transition (EMT) followed by extensive migration towards a variety of target tissues, where the NC cells differentiate into more than thirty different cell types, including peripheral and enteric neurons and glia, craniofacial osteocytes, chondrocytes, adipocytes and mesenchyme, chromaffin secretory cells and pigment cells.

Neural crest biology has been scrutinized during development and evolution, leading to the elucidation of elaborate gene regulatory networks (GRNs) during the last decade (*9*, *10*). These networks, however, remain incomplete and do not account for most of the defects observed in human neurocristopathies (*11*). This problem is ripe for single cell (SC) transcriptomics which would enable a full description of NC development, over sequential developmental stages, and in comparison to adjacent tissues (e.g. at the neural border) would define the developmental genetic trajectories of the complete NC lineage tree. Recent SC studies on NC cells have mainly explored NC after emigration, using chick, fish and mouse embryos (*12*) (Supplemental Table 1). In contrast, pre-migratory NC single cells have received limited exploration, mostly around the EMT stage and on small cell numbers at a specific level of the body axis (*7*, *13*). While the formation of the NB territory has been defined by expression of a few genes during gastrulation (e.g. *pax3* and *pax7)* (*2*, *9*, *14*), the timing of NB specification from the rest of the dorsal ectoderm and the circuits driving fate decisions between the four NB-derived cell fates (NC, placodes, non-neural ectoderm and dorsal neural tube) remain to be established (*3*, *15*, *16*). Furthermore, the timing of lineage decisions in the pre-migratory NC along the anterior-posterior axis, the maintenance of a multipotent NC sub-population, and the molecular mechanisms driving each state of the pre-migratory NC lineage tree remain unexplored. Here, we used single cell transcriptomes from eight consecutive developmental stages of *Xenopus tropicalis*, featuring 6135 NC cells and 17138 early ectoderm cells, to provide a comprehensive developmental profiling of the NB and the pre-migratory NC. We have uncovered several new NC sub-populations and highlighted their precise trajectories, resulting in eight NC sub-populations emigrating from anterior to vagal levels of the body axis. Interestingly, we find that some fates emerge much earlier than previously anticipated, that NC diversity is maintained upon EMT and that further diversification occurs at the onset of migration. We propose a temporal sequence of molecular events underlying the successive transcriptomic states and the fate decisions supporting the emergence of the NC cells from the neural border during gastrulation up until early migratory states at early organogenesis stage. Moreover, we identify key transcription factors involved in main lineage branching and validate several regulatory predictions *in vivo*. We therefore provide an extensive gene regulatory network describing the emergence of the neural crest lineage in the ectoderm of vertebrate embryos.

Results

General strategy for identification of neural crest and neural border zone cells.

Using deeper re-sequencing of single cell (SC) series from whole *X. tropicalis* embryos (*17*), taken at 8 consecutive developmental stages, followed by updated genome annotation and alignment, we have scrutinized 17138 early dorsal ectoderm cells and 6135 neural crest (NC) cells from early gastrulation stage to post-EMT early migration stage. The large cell number of our new dataset permits assessment of the cellular diversity in the NC population during early induction (at late gastrulation stages 12-13 and neural plate stages 13-

14), during neural fold elevation (stages 16-18), during EMT (neural tube stages 18-20) and at the earliest stages of NC cells emigration (tailbud stage 22).

During gastrulation (stages 11-13), the neural plate and the neural border zone are induced from the dorsal ectoderm due to BMP antagonists in the midline and Wnt/FGF signaling from the underlying mesoderm (*18*). As early as stage 10.5-11, the neural border initiates a few distinct gene expressions, such as *pax3/7* (*19*). However, a fuller definition of the NB transcriptome is still lacking. Unlike the neural border, the neural crest has long been defined by the expression of a set of typical genes, like *snail2*, *sox8/9/10*, and *foxd3*. Previous RT-qPCR or *in situ* hybridization showed *sox2* (neural), *snai2* and *sox10* (NC) expression at stages 11, 12 and 14 and expression of other NC markers used for cell selection (*sox8*, *sox9, zic1*; Fig. S1). Importantly, we detected the regional expression of such ectoderm genes in SC data at similarly early stages. This sensitivity was essential to capture the emergence of rare gene programs.

We first performed unsupervised clustering of the whole embryo dataset at each stage (a total of 177250 cells) and identified the NC clusters by expression of canonical NC genes, from induction (stage 12) to migration (stage 22) as well-established in the literature (Figs. 1A, S1; Table S2 and Materials and Methods). We next defined the genes most specific for NC and expressed broadly across the NC population, by selecting genes with high NC-specificity scores compared to the rest of the embryo, and low variation within the NC population. This highlighted *tfap2b, c9, c3* and *sox8* as the best pan-NC markers during neurulation, closely followed by *snai2* and *sox10*. Small temporal variations in these genes' expression suggested that early NC is best labeled by *snai2* at stages 13-16, followed by *tfap2b* from stage 14 to 20, or *c3, c9, sox8* between stages 14 to 18 (Figs. 1C, D, S1). However, in addition to being broadly expressed in the NC cells, *c3* and *c9* are also expressed in placodes and some ectoderm cells (Fig. 1D). This points to *tfap2b* as the most specific pan-NC gene shortly prior to EMT, an important notion for future selection of NC reporters for transgenesis.

We validated the NC selection method by designing a LightGBM (*20*) NC classifier. We tested it on another vertebrate organism, zebrafish, to evaluate its accuracy for NC annotation. Our binary classifier determined whether a cell was NC or not, using our annotated frog whole embryo dataset at seven developmental stages (12-22). The algorithm was tested on a zebrafish whole embryo SC dataset (*21*) at stage 14hpf (equivalent to frog stage 22) with a result of 0.95 for AUC score and 0.66 for F1 score (F1 score defines the weighted harmonic mean of the precision and recall, and it is equal to 0.05 for a random model applied to the zebrafish dataset, Fig. S2). This result was striking because it was robust despite significant species-specific variations in the expression of classical NC gene markers between frog and fish, and despite a strong batch effect between the datasets (595 genes from the list of the most important genes for NC classification were missing from the zebrafish dataset). For example, the expression of *c9* and *snai2,* which are pan-NC genes in *Xenopus,* was drastically different in the zebrafish NC dataset. Yet, the classifier efficiently recognized NC cells in the fish neurula. This result confirmed the accuracy and robustness of our NC cells selection criteria.

While the identity of early NC cells has been well described, very few NB-specific markers have been identified (e.g. *pax3/pax7* in frog and chick respectively) (*2*). The NB zone has instead been defined by the *overlapping gradients* of ectodermal expression of ventral-lateral genes (e.g. *msx1, tfap2a, hes4, tfap2a)* and dorsal-lateral ones (e.g. *zic1, zic3)*, and by the early *exclusion* of ventral-most non-neural ectoderm marker expression (NNE, e.g. *dlx3, foxi1e, ker81)* and dorsal-most neural plate ones (*sox2)* (*22*, *23*). We have thus identified NB cells as the group of cells co-expressing *zic1* (dorsal and NB marker) and *tfap2a* (ventral and NB marker) simultaneously at high levels (*19,* see Materials and Methods). Differential

expression analysis with both neural and non-neural progenitors revealed a clear NB gene signature enriched for *sox9, pax3, snai1/2, hes1, gmnn, lhx5* and *axin2* expression. NB zone differential analysis with neural crest and placodes revealed NB-specific expression of *has1, lhx5* and *tfap2c* genes. This indicates that the NB territory, which was so far mainly defined by the overlap between several gene patterns, also presents a specific identity from gastrula stage 11 (Fig. 1B, E). Thus, we have determined a clear signature of developing NC progenitors from stage 11 to stage 22.

Single cell heterogeneity of premigratory cranial and vagal neural crest during neurulation reveals early lineage diversification from an unbiased stem cell population which persists throughout EMT.

Next, we used Leiden clustering (*24*) on the principal component derived neighbor graph to separate the NC cells into distinct states. We defined the optimal number of clusters by manually increasing their number and checking for biological meaning, as revealed by specific gene expression, for example of *hox* genes, such as *hoxd3* for cardiac NC (cluster #12), or *hoxb6* for Enteric Nervous System progenitors (ENSp, cluster #13). We defined 16 clearly distinct states with specific gene signatures, compared to 8 states previously described in (*17*) (Fig. 2A, C, E). Using partition-based graph abstraction (PAGA) analysis (*25*), we described the principle graph of similarities between clusters' transcriptomes (Fig. 2B). This revealed the complexity of interconnections between each cluster from early neurulation to emigration stage.

In this cluster map, we first searched for NC cells emigrating from the neural tube, which are the best characterized so far. We identified 10 cell clusters with an explicit mesenchymal NC signature (#12, #9, #15, #11, #7, #16, #8, #14, #13, #6, all expressing various levels of *itga4*/integrin-a4, *vim*/vimentin and *fn1*/fibronectin, Fig. S4)**.** These clusters mainly included stage 18 to 22 “late” cells (Fig. S4), stages when the cranialmost NC undergoes EMT and early migration. Using their *hox* gene expression signature, we positioned these clusters along the body axis (Fig. 2D). We also identified five cranial NC cell subpopulations devoid of *hox* gene expression. Three were previously found in (*17*): #10 (*rpe65*$^{+}$*, zfhx4*$^{+}$*, alx1*$^{+}$ NC); #11 (*vim*$^{+}$*, itga4*$^{+}$ enriched NC) and #15 (*dlx2*$^{+}$*, efnb2*$^{+}$*, cyp26c1*$^{+}$*, epha2*$^{+}$ NC) (Fig. 3A). Additionally, we uncovered two previously undescribed clusters: #16, a muscle-like NC subpopulation, expressing actin and myosin-like genes (*actnc1*$^{+}$*, myl1*$^{+}$ cells) and #14, a cluster of migrating NC cells expressing the canonical early neural crest signature (*tfap2b, c9*) without additional specific gene expression, suggesting that these cells continue to remain unbiased and are potentially multipotent (Fig. 3B-D, F). Finally, we identified three subpopulations of *hox*-positive rhombencephalic neural crest previously grouped together (*17*). These cells form clusters #12, #13 and #9 and express *hoxa3, hoxb3, hoxd3* and are thus located at the vagal level. Cluster #12 includes cardiac NC (*egr2*$^{+}$*, mafb*$^{+}$) (*26*) while cluster #13 contains (*tnc*$^{+}$*, ltbp1*$^{+}$) ENS progenitors (*27*).

Characterization of a new migratory muscle-like NC cluster.

One key expectation from single cell transcriptomics is to identify and characterize novel rare cell states. Here, cluster #16 describes the emergence of a muscle-like NC subpopulation, previously undescribed at the single cell level and expressing simultaneously late pan-NC markers (*tfap2b, tfap2e, sox10, c9*) and muscle markers *actc1, myl, mylpf, cstb* and *des* (Figs. 2, 3F, S3*). Myl1* is expressed in striated muscle (*28*) and future lineage tracing analysis will determine if these cells generate NC-derived myofibroblasts or striated head muscles. To validate this finding biologically, we have used a well-established assay in *Xenopus laevis* embryos, using pluripotent ectoderm that can be directly reprogrammed into into neural crest progenitors, without any mesodermal contribution (induced neural crest assay, Fig. 3E) (*29*). The explanted ectoderm form spheroids that were cultured until the

equivalent of stage 20-22. We found that *myl1* and *myoD* started being expressed around stage 20 from the induced NC progenitors (Fig. 3F). This finding complements the palette of differentiated phenotypes elicited by this assay, and opens future avenues to study these NC-derived muscle cells.

This muscle-like cluster #16 was the only NC cluster to initiate differentiation. While it has been proposed that the melanocyte lineage was biased prior to NC emigration from the neural tube, we did not see a specific set of cell states that would support pre-migratory melanoblast formation, even rare ones, in our dataset (e.g. no significant detection of *dct, tyr, tyrp1* expression) (*30*). This led us to propose that our global analysis found no other indication of cell fate determination until stage 22 at cranial and vagal levels, in agreement with previous single cell lineage-tracing studies (*31*).

Developmental series analysis reveals that some NC states are generated over long time periods.

The second asset of this dataset is that it follows the cell states over a developmental time series. We could thus assess not only “pseudotime” trajectories (reflecting the heterogeneity of closely related cell transcriptomes at one time point) but also "real time" population dynamics for each cluster in the embryo. Indeed, each cluster is composed of a variable number of cells from different developmental stages, indicating that a given transcriptome state is reached by different cells over time (Fig. S4A). Because each state is characterized by a *hox/non-hox* signature, as an estimate for the cells’ position along the body axis, surprisingly these temporal variations do not describe the anterior-posterior wave of NC cell emergence (Fig. 2A). Rather, the range of stages found in each cluster describes the time period over which each regional state of the NC-GRN is generated. For example, cluster #10, which gathers cranialmost NC cells, is generated over the entire duration of neurulation starting at neural plate stage 13, with most cells ranging from mid- to late- neurula stages 14-16-18, and even persisting after EMT stage during stages 20 and 22. This reflects how NC cells of a similar state can be continuously generated over the course of development at a given portion of the neuraxis. In contrast, clusters #11 and #15, two migratory clusters highly expressing *vimentin (vim$^+$),* are generated abruptly at one single post-EMT stage (stage 22) and eventually populate cranial areas as well. These could reflect an abrupt step of mesenchymalisation in the epithelial-to-mesenchymal transition process of cranial NC.

An unbiased NC state coexists with diversifying states upon EMT.

The third major advantage of this dataset is its high cell number, likely to capture most, if not all, cell states during NC formation. This allowed us to find a group of NC cells with immature/pan-NC signature that persists throughout neurulation and EMT. At EMT/migration stage, cluster #14 expresses the canonical early neural crest signature (*tfap2b, c9*), as well as *mmp14* but low *vim, twi1,* and *fn1*. This cluster includes a variety of developmental stages (from stage 13 to 22) and represents a potentially “multipotent” stem-like NC cluster (Figs. 2A, 3B-D). We thus addressed whether all NC cells adopted a similar unique “stem-like” state upon EMT as it was proposed recently (*13*). Instead, we observed that the list of clusters with elevated expression of *vim, fn1*, and *mmp14* possessed distinct features: for example, clusters #10, #13, #15, are all undergoing transition to a mesenchymal *vim*$^+$ state but #10 and #15 are ecto-mesodermal (*twi1*$^+$), while *#13* instead highly expressed *tnc* (Fig. S3B, C). None of these three clusters are similar to stem-like cluster #14. Clearly, the diversity of states is maintained as cells transition from pre-EMT stages to EMT and early migration. In conclusion, by exploring a high-density dataset, we did not see that NC cells adopt a single homogeneous state upon EMT, but rather continue to remain highly diverse.

In summary, our data describes the NC cell populations along a significant segment of the body axis, from the anteriormost cranial NC to the vagal level. We find three important novel points characterizing NC cells around the time of EMT and initiation of migration. Firstly, there is a large diversity of states along the cranio-caudal axis. This diversity comes from cells adopting specific states, such as different cranial populations, multipotent-like state, enteric nervous system progenitors, at different time points during development, with some early-stage cells being intermingled with later ones into the same cluster. Secondly, state diversity is maintained as cells undergo transition from epithelial to mesenchymal phenotypes, while a stem-like subpopulation persists as a distinct cluster. Lastly, we identify a myoblast/myofibroblast-like cell population with strong NC stem-like features as the first one to differentiate upon EMT, but we do not detect indications that other NC derivatives would be set aside from the main premigratory NC population prior to or upon EMT.

A comprehensive lineage tree of cranial and vagal NC cells from induction to migration reveals early developmental heterogeneity dynamics and the maintenance of a stem-like NC population throughout neurulation.

With reference to the post-EMT NC clusters, we were able to define eight progenitor states for NC cells. These delineate developmental dynamics of cranial, vagal and enteric nervous system progenitors. These clusters mainly include cells from the second part of gastrulation (stage 12) to pre-EMT stage (stage 16). Unexpectedly, as early as at gastrula stages 12-13 we detected three NC cell states clearly distinct from the main early NC state: an *hnf1b*$^{+}$ cluster #3, a *cyp26c1*$^{+}$ cluster #4 and and *rpe65*$^{+}$ cluster #10 (Fig. 3A). However, these clusters only comprised small cell populations while most cells in stages 12-13 bear an "unbiased" canonical early NC signature: 85% for stage 12 and 68% for stage 13 (Fig. 3B). At mid-neurula stage 14, two additional trajectories emerge from the unbiased stem-cell like lineage, *nrp2*$^{+}$ cluster #7 and *mafb*$^{+}$ cluster #9. Using these specific signatures, we described the main characteristics of progenitors for each cranial to vagal NC subpopulation.

Three early premigratory states emerge at the end of gastrulation.

From the earliest stage of NC induction, three distinct trajectories emerged from the main canonical NC progenitor population (Fig. 2). First, the previously undescribed *hnf1b*$^{+}$ cluster #3 is a pre-migratory cluster composed mainly of stage 12, 13 and 14 cells expressing pan-NC markers such as *pax3, tfap2b* and *sox9,* as well as the dorsal neural gene *olig4, hnf1b,* the *ngfr*-related gene *nradd*, complement factor *cfb,* the posterior master regulator *cdx4* and a strong posterior hox gene signature (including posterior hox gene *hoxb8* and sacral hox genes *hoxc10/hoxd10*) (Figs. 2D, S3). Interestingly, this cluster seemed to respond to a combination of high WNT/low RA signals, in line with its posterior trunk fate specification (*32*). Indeed, early on, cluster #3 expressed canonical WNT signaling targets *axin2* and *cdx4* (*33*), as well as *dhrs3*, which attenuates RA signaling, is required for posterior axis formation and is usually mutually exclusive with *cyp26c1* expression (Fig. S3B, S5C) (*34*). In cluster #3's older cells, expression of genes responsive to canonical WNT signals, *cdx4* and *sp5,* was decreased, while expression of the non-canonical ligand *wnt11* was increased. Cluster #3's trajectory converged and merged with the enteric NC cells of cluster #13. While most of the enteric peripheral nervous system (ENS) arises from vagal NC, sacral NC cells contribute to cells in the hindgut. Cluster #3 posterior gene signature suggested that as early as mid-gastrulation stage 12, a minor NC progenitor population is already biased towards the future sacral NC fate, although those cells would emerge later on from the neural tube at tailbud-stage and give rise to the posterior ENS (*35–37*). Moreover, *wnt11* negatively regulates enteric NC differentiation (*38*), further suggesting that cluster #3 trajectory may consist of immature ENS progenitors. This cluster is the most posterior cell group found in this dataset (posterior trunk/sacral *hox* signature). Identification of cluster #3 specific markers will enable future lineage tracing

experiments to define the position and developmental contribution of these early progenitors of the enteric nervous system.

The second early-biased cluster, cluster #4, was composed of neural plate stage 13-14 progenitors of cranial NC populations with a unique retinoic acid (RA) signaling-related signature. It merged with cluster #6, (composed of stage 16-20 cells) and cluster #15 (composed of stage 22 cells). Cluster #4 specifically expressed genes encoding the RA-degrading enzyme *cyp26c1,* transcription factors *meis2* and *olig3,* neuropilin receptor *nrp1,* ephrin signaling receptor *epha2,* and ligand *efnb2* (Fig. 5S). Compared to the early unbiased cluster #1, cluster #4 exhibited increased expression of mature pan-NC markers *tfap2b, c9, snai2*, and decreased expression of multipotency marker *pou5f1* (Fig. 3D). Cluster #4 expressed *hoxb1* and *hoxb2* indicating an anterior rhombencephalon position. More precisely *epha2* expression pinned those cells to rhombomere 4 (Fig. 2D) (*39*). High *cyp26c1* expression indicated low RA levels as essential to define rhombomere 4 identity (*40*)**.** Last, *nrp1* specifically marks mouse NC from rhombomere 4 suggesting high conservation of the cluster signatures across vertebrates (*41*). Cluster #4's *cyp26c1/epha2* signature remained specifically expressed in the low-RA-dependent stream (#6, #15) from stage 12 to 22. Expression levels of genes encoding *epha2* and *efnb2* remained high while *cyp26c1* expression gradually decreased in later subpopulation of posterior CNC along with increased expression of genes encoding RA receptors (*rarg, rxrb, ncor1*; Figs. S5A, B) and cellular retinoic acid-binding protein 2 (*crabp2*). This revealed that the identity of rhombomere 4 NC was established as early as neural plate stages 13-14 under low RA signaling (cluster #4) while starting at neural fold stage 16 (cluster #6), later development of this lineage involved increased RA signaling. These observations highlighted the transcriptional outcomes of dynamic RA signaling in the progenitors of rhombencephalic neural crest forming the first (mandibular) and second (hyoid) arch stream respectively, anterior to the otic vesicle.

Appearing at stage 13, the third early-biased cluster is *hox*$^{-}$ cluster #10, expressing *dmbx1, otx1, nrp2, lmx1b, rpe65* and *pax3,* thus containing premigratory early cranial cells (Fig. S3A). Bias towards cluster #10 was slightly noticeable at stage 12, as around 5% of the *unbiased* cluster #1 co-expressed *dmbx1* and *otx1*, which might indicate early fate predetermination. Moreover, 10% of the cluster *#10* were cells of 13-14 stages (Fig. S4A), the rest being later stages. Lxh5 and Dmbx1 are early cranial NC-specific factors and drive expression of *tfap2b* and *sox8* (*10*). Here we found *lhx5* and *dmbx1* expressed separately in early unbiased cluster #1 and in cranial cluster #10 (Fig. S5D), and confirm *otx1* as a marker for anterior neural border (*2*). This means that progenitors for cranial NC start being specified at neural plate stage, much earlier than anticipated.

Two bipotent clusters appear at mid-neurulation stage forming cardiac, enteric and cranial progenitors

Two clusters were composed of progenitors for more than one trajectory ("bipotent clusters"): a partially biased vagal cluster #9 (*mafb*$^{+}$) resolving into both the cardiac NC cluster #12, and the ENSp NC cluster #13, and a cranial cluster #7 (*nrp2*$^{+}$), which is equally linked to the *rpe65*$^{+}$*, zfhx4*$^{+}$ cluster #10 and to the *vim*$^{+}$*, itga4*$^{+}$ enriched cluster #11 (Fig. 2C). From late neural plate stage 14, the unbiased cluster #5, with higher expression of *c9, sox8, tfap2b* in comparison to the earliest unbiased cluster #1, started to split into the vagal-biased #9 (*mafb*$^{+}$, *hoxd3*$^{+}$) and the cranial-biased #7 (*rpe65*$^{+}$*, dlx2*$^{+}$*, hox*$^{-}$) trajectories. Despite the global homogeneity within cluster #5, we detect a slight stratification for expression of neuropilins *nrp1* and *nrp2*, which would later mark NC cells emigrating from rhombomere 4 and from rhombomere 2 respectively (*41*). This suggested that within the unbiased cluster #5, a few cells initiated a trajectory towards cluster #9 (vagal NC, *nrp1, mafb*, *cfi*, *meis2*, *mdk*) while others are shifted towards an anterior hindbrain trajectory (*nrp2*, *id3*, *ifitm3*, *alk;* Fig.

S9A, B*)*. This indicated that the SC transcriptomes identified an early bias in "bipotent" cell populations, enabling analysis of gene regulation during specification of each fate.

The multipotent NC gene signature identifies a separate cell lineage from neural plate stage to the onset of migration.

During the whole process of neurulation, from NC induction to NC migration stage, a significant proportion of the cranial and vagal NC progenitors expressed a canonical NC stem cell-like signature (*sox9, tfap2c, snai2)*, together with high expression of pluripotency markers (*e.g. pou5f1*, *cmyc*, and *sox2).* No indication of bias towards a specific fate/alternative state was detected in these clusters (#1, #5 and #14) (Fig. 3B-D). The signature of these potentially multipotent cells, consisted of transcripts common to all NC cells, but was slightly variable across stages. At induction stages, this cell lineage expressed enriched levels of *zic1, zic3, tfap2c, cldn6* and *c3*, while at stages 18-22, it was enriched for *tfap2b, mycn, eef1b2, apoc1, vim, rack1, tfap2e* and *c9* expression. About 72% of NC progenitors were found unbiased at induction stages (gastrula and neural plate stages 12-14), 15% at pre-migratory and EMT stages (stages 16-18) and 9% among tailbud stage 22 NC cells. Interestingly, according to PAGA, the latest unbiased population (#14) is transcriptionally equally close to the vagal (#9) and cranial (#7) transitional clusters described below, indicating that some stage 18-20-22 cells share the unbiased pan-NC signature irrespective of their cranial or vagal levels of origin. Moreover, the whole unbiased lineage (clusters #5, #14) is mostly composed of premigratory cells with low *vim/fn1* expression and remains *hox* negative, generating NC cells which acquire a *hox* signature upon emigration state (*e.g.* hindbrain cluster #15 expressing *hoxa2*).

In sum, this detailed cluster analysis provides the temporal dynamics of gene expression underlying the main transcriptional states defining the various premigratory neural crest trajectories (Figs. 2, S3A). It highlights the early specification of several lineages, along with the maintenance of a NC stem-like population at all axial levels between cranial and vagal body axis regions. This analysis further provides a basis for the in-depth exploration of gene program variations which may drive branching at each bifurcation.

Connectome analysis

Connectome predictions using GRNboost2

Using the temporal dynamics of gene expression, several algorithms have been designed to infer genetic co-regulation (*42*). One of them, GRNBoost2, is based on a gradient boosting machine and retrieves the gene regulatory network (GRN) from the expression data-matrix (*43*). Starting from a given list of TFs, this algorithm powerfully links genes with similar expression patterns in SC transcriptomes, providing “syn-expression groups” (*44*) at the single cell level. Thus, GRNBoost2 provides a network of potential bidirectional gene relationships (including genes encoding TFs and other types of proteins). To expand significantly the network of genes involved in the NC/NC progenitor GRNs, we used an input list of 1417 TFs (*45*) and applied GRNboost2 on the NC dataset. After filtration by expression levels and edge weights (predicted importance of the connection), we retrieved 16978 TF-target connections defining a global NC network with a median 22 connections per TF (Fig. 4A). To define the main GRN nodes (= genes), we calculated the number of connections per gene (*degree centrality*) and the degree to which a gene lies on paths between other genes (*betweenness centrality*). Further, we determined the main nodes for each developmental stage using nodes maximal expression (Table 1). Among the genes predicted to be important at NC induction stages, we retrieved the previously known early neural border specifiers *pax3* and *zic1*, as well as *zic3, olig4, sox9*, and the anterior NC marker *dmbx1*. For premigratory NC stages, the model predicts prominent functions for the known NC specifiers *tfap2b, sox10 and snai2*, the anterior NC markers *rpe65* and *alx1*, and for the hindbrain hox gene *hoxb3*. At the

stage of NC cell migration, *tfap2e*, *mycn, dlx2* and *egr2* (*krox20)* displayed high expression and high degree centrality. This analysis thus retrieved several known key regulators in the NC-GRN (*pax3, zic1, sox10, snai2 etc.)*, validating the pertinence of the model, while also predicting strong new candidates (Table 1).

Large scale experimental validation of GRNboost2 model predictions

GRNboost2 is currently one of the best GRN predictors (*42*). However, benchmarking with experimental datasets is still lacking. In order to validate experimentally the network predicted with GRNboost2 in the TF-towards-gene-target direction on a large scale, we sequenced NB/NC microdissected explants after genetic perturbations (Fig. 4A, B). We depleted selected gene products *in vivo* using previously validated antisense morpholino oligonucleotides (MO) designed against *pax3* or *zic1* (Pax3 MO*,* Zic1 MO) (*9*). At mid-neurula stage, individual wild-type, Pax3-, or Zic1-morphant explants were microdissected from the anterior NB ectoderm (aNB) using sibling embryos and processed for small-RNAseq [as in (*2*)] (Fig. 4B). Differential analysis found decreased expression of 1333 genes in Pax3 morphant NB and 1103 genes in Zic1 morphant NB respectively (Figs. 4B, S6). This confirmed that these two NB specifiers are essential to activate a large NB/NC gene signature, and provided the most complete list to date of Pax3 and Zic1 targets in the premigratory neural crest (Tables S3, S5). We found that GRNBoost2 predicted 1076 genes to be linked to Pax3 activation, among which 170 were decreased in Pax3 morphant neural crest (e.g. *zic1*, *knop1*, *bms1* and *prps1*, Figs. 4B, S7). Similar modelling predicted 1136 genes linked to Zic1, of which 188 were significantly changed in Zic1 MO cells (Figs. S6, S7). Interestingly, *cyp26a1* was connected to *zic1* in the predicted network and was significantly decreased in Zic1 MO. This supports previous characterization of *cyp26c1* as an immediate-early target of Pax3 and Zic1 (*46*), and may relate to potential roles of Zic1 and Pax3 in antero-posterior patterning through regulation of retinoid signaling (*47*).

We further defined Pax3 direct binding on target genes *in vivo* using ChIP-seq (Fig. S8) on mid-neurula stage embryos (Fig. 4D). We retrieved 475 targets of Pax3 expressed in the SC NC dataset, among a total of 657 targets found in the whole embryo (Table S6). Known targets such as *cxcr4* and *prtg* were validated (*46*, *48*). Among the 475 targets, 80 were also predicted by GRN-Boost2 modelling including *psmd4, psen2, sp7, notch1, hnf1b.* In sum, we provide here a vast Pax3-centered NC-GRN with three complementary approaches: GRNboost2 predictions, morpholino-based depletion and Pax3 chromatin-binding (Fig. 4B-D). However, the overlap between the gene lists retrieved as targets by three approaches was only partial. A first possible reason is that GRNBoost2 predicted a larger group of connections than did experimental MO depletion-based small-RNAseq or ChIPseq: based on gene expression patterns, GRNBoost2 retrieved both TF-towards-target and target-towards TF potential relationships. Another possibility is that the *pax3* expression pattern, used as the basis for GRNboost2 predictions, is broader than most NC specifiers' early pattern [see in (*2*)], as *pax3* is also expressed in the prospective dorsal neural tube, for example in stage 12-13 neuroepithelial cells (see ectoderm cluster #7, #9 below). Nonetheless, these data provide a NC-specific genome-wide connectome for two key NB specifiers, Pax3 and Zic1, much of which we have validated experimentally.

We next focused experimental validation on a later NC specifier, TFAP2e, highly expressed in cranial and trunk NC cells at a late neurula stage, predicted to be an important node at EMT stage 19 (Fig. S9D). Using a similar approach, we processed for small-RNAseq pre-migratory NC explants microdissected at the end of neurulation (stage 17-18) from wild-type or *tfap2e* morphant embryos (Fig. S6) (*49*). Among 848 targets of TFAP2e predicted by GRNBoost2 from scRNA-seq, 99 showed decreased expression after TFAP2e depletion in NC *in vivo* (e.g. *tfap2b, sox10, dact1, sncaip;* Figs. 4E, S7). Moreover, using ChIP-seq for TFAP2e, we identified 642 targets expressed in the NC dataset, among 805 targets for the

whole embryo, including top-scored *rmb20, pim1, arl5b* and *tfap2a* (Fig. 8S, Table S7). Out of 848, 76 genes linked to *tfap2e* by synexpression analysis were directly bound by TFAP2e in the late neurula *in vivo*. Thus, we also provide here a large-scale TFAP2e-centered NC-GRN using GRNboost2-predicted, morpholino-validated and ChIPseq-validated targets.

Benchmarking SC-based machine-learning and in vivo experimental approaches to build the neural crest GRN.

Our SC analyses provide a genome-wide connectome based on a total of 16978 interactions computed between 405 TFs (out of the initial list of 1417 TFs expressed in developing embryos) and 4532 other genes expressed in neural crest during gastrulation and neurulation. The biological significance of the network was validated using experimental analysis for three different NB/NC specifiers, Pax3, Zic1 and TFAP2e, as transcriptomic interactions predicted using GRNBoost2 retrieved many interrelations supported either by direct TF binding (ChIP) or by TF depletion *in vivo*. However, when comparing the targets predicted with SC transcriptome modelling and experimental validation *in vivo*, we find that the fraction of gene correlations predicted with GRNboost2also validated by ChIPseq was 7-9%, and also confirmed by TF depletion (which includes both direct and indirect targets) was 11-16%. Changing the network filtration criteria (weights, expression level) did not affect the proportion of validated genes. This means that despite the significant discovery power displayed by GRNBoost2 on a complex dataset, there is margin for increasing its specificity and accuracy. For example, GRNBoost2 did not link *tfap2e* to *hnf1b* (although confirmed by both ChIPseq and MO depletion), possibly because those genes have quite different expression patterns during the course of neurulation (Fig. S9D). Likewise, GRNBoost2 did not link *tfap2e* to *notch1* either (also confirmed with ChIPseq and MO) although they display closely related patterns (Fig. S9D). Another hypothesis for the incomplete coincidence of the predictions between MO/ChIP and GRNboost2 is that the dataset compiled for GRNboost2 includes cells of all available stages (due to the need for a large number of cells for modelling) while the MO/ChIP experiments were carried out at specific stages. Additionally, another limitation of GRNboost2 is its weak ability to predict the relationship between genes with different expression time-frames, i.e. when a gene A activates a gene B and stops being expressed in B-expressing cells. In this case, it is best to apply a branching analysis taking pseudotime into account. Yet, these three TF-centered networks exemplify how a large single cell dataset can be combined with *in vivo* experiments and bulk small-RNA-seq to efficiently identify a substantial number of novel interactions in the NC-GRN: we provide here 264 targets of Pax3 in NC, covered by at least two methods, 206 for TFAP2e and 188 for Zic1 (Fig. S8). To further render this extensive resource available, we provide an interactive visualization tool of all the interactions predicted between TFs and tables with their targets validated with ChIP-seq and MO-based small-RNAseq (available upon publication).

Branching towards biased premigratory neural crest is controlled by key transcription factors.

To explore the temporal dynamics of transcription factor expression that may specify decision points in the development of pre-migratory neural crest, we used tree inference and advanced pseudotime downstream analysis, with a focus on fate biasing using scFates (*50*). It allowed us to explore the branch-specific transcriptional regulation from the calculated pseudotime, in order to determine not only the gene-to-gene dependency but also the temporal order in which their functions were accomplished. ElPiGraph approximates datasets with complex topologies allowing us to build the graph structure. One limitation of ElPiGraph is that it cannot be applied to large datasets with many potential branches. Thus, using the principal graph constructed with PAGA (Fig. 2B), we sub-selected cells around three main bifurcation points in the NC lineage tree and applied scFates, ElPiGraph and differential expression analysis. We explored firstly the split of trajectories from Premigratory Unbiased

NC (cluster #5) to Migratory Bipotent Cranial NC (cluster #7) and Migratory Bipotent Vagal NC (cluster #9); secondly the bifurcation of Migratory Bipotent Vagal NC #9 into EMT Cardiac NC (#12) and Migratory ENSp (#13), and thirdly the emergence of two distinct cranial states, Premigratory Early Cranial #10 and Migratory Cranial #11, from Migratory bipotent cranial cluster #7 (Fig. 5A-F).

Cranial versus vagal bifurcation at the end of neural plate stage.

Cranial NC cells emerge from the neural tube anterior to the otic vesicle while vagal NC cells form from the hindbrain region adjacent to somites 1–7 (*51*). Our data indicates that the first emergence of cells biased to vagal and cranial populations arise from the unbiased population of cluster #5 around early neural fold stage 14. Although we did not see separation of cluster #5 into two populations at the chosen level of clustering, we still observe an early internal predisposition marked by the expression of early cranial (*nrp2)* and vagal (*mafb*) markers in sub-regions of cluster #5 (Fig. S9A, B). In this analysis, cells that express *nrp2* highly were closer to the cranial state than to the vagal stage (7 times more according to PAGA; Fig S9A, B). Similarly, we explored cluster #5 cells which highly express *mafb* and found them 1.5 times closer to the vagal state than the cranial state. Thus, although cluster #5 is rather homogeneous, a few genes might be responsible for early predisposition to the vagal or cranial fates as early as stage 13. Moreover, we found that *mafb* and *nrp2* were the best early predictors of branching for the vagal and cranial populations (Fig. 5A, B). Using branching analysis, we retrieved early vagal gene programs as the sets of genes activated before bifurcation (early; *mafb, klb, mdk*) and continuing to be expressed in each specific branch (late; *prdm1, cfi, hoxd3*) (Fig 5A). Similarly, we uncovered early (*nrp2*, *alk, rnd1, adam19*) and late (*shisa3, frmd6*) gene programs for cranial NC cells of cluster #7 (Fig. 5B). This is in line with previous *in vivo* analysis of Alk function in cranial NC cells before and during migration (*52*) and of Mafb role during cardiac NC cells specification (*26*).

Neural fold stage bifurcations: vagal to enteric split and cranial subdivision.

We also defined gene programs for two later bifurcations: early vagal NC progenitors of cluster #9 bifurcating into ENS (cluster #13) and cardiac NC (cluster #12) on one hand, and bipotent cranial NC (cluster #7) bifurcating into *rpe65*$^{+}$ Cranial NC cells (cluster #10) and Migratory Cranial *hox*$^{-}$; *dlx2*$^{+}$ NC cells of cluster #11 on the other hand. In contrast to the unbiased cluster #5, clusters #7 and #9 are relatively homogeneous without obvious propensity towards other later cell states. However, branching analysis revealed clear early and late branch-specific actors. For the cardiac NC fate, we defined early genes, *mafb, mycn, prdm1, nolc1* and *eef1d* and late ones, *egr2, hoxd3, epha4* and *abtb2*. For enteric nervous system precursors (ENSp), early actors were *olig4* and *fbn2*. Due to its significantly increased expression in later ENSp cells, the branching analysis identified *pax3* as a late actor, but the expression-pseudotime heatmap showed that *pax3* was already expressed prior to branching in ENSp progenitors and increased afterwards (Fig. 5C). Therefore, we also assigned *pax3* to the group of early genes for ENSp. Later ENSp gene programs consist of *tnc, ltbp1, wnt11,* and *hoxb6*. In order to validate experimentally if "early" factors affected "late" genes expression, particularly if early TFs were bound to the late genes sequences, we examined which of the late ENSp genes were targets of the early TF Pax3 gene, by ChIP-seq and MO analyses. We identified several genes affected by Pax3 depletion, among them *krt8* (increased), *cldn1* and posterior hox genes *hoxb6* and *hoxa7* (decreased) (Fig. 5G) while several were identified as direct targets of Pax3 (e.g. *cfb* and *bmp5*, Figs. 5G, S9C).

Last, similar analysis on clusters 7-10-11 showed that early genes specific for Premigratory Early Cranial cluster #10 branch were *rpe65, dmbx1, rgr, lmx1a,* and *zfhx4*, while late gene programs consisted of *alx1* and *bmper* (Fig. 5E, F). Interestingly, we found *pax3* expressed early in cranial bifurcation from #7 towards #10 and #11. *Pax3* was expressed

in cluster #7 progenitors and specifically enriched in *rpe65*$^+$ cluster #10. To explore this further, we also used ChIP-seq and MO to determine if there were cluster #10-specific genes among Pax3 direct targets and found that *comt, slc23a2* and *rpe65* were affected after *pax3* depletion while *bmper, f10, sema3a, dmbx1, slc16a12* and *kif26a* were directly bound by Pax3 (Fig. 5G). On the other hand, the branch leading to Migratory Cranial *hox*$^-$*;dlx2*$^+$ NC cells (#11) expressed *mef2c* and *eef1d* before and after bifurcation, and *dlx2, shb, itga4* only after bifurcation. We found that *tfap2e* started to be expressed before bifurcation and was enriched in cluster #11 in comparison to cluster #10. Consequently, using MO-mediated depletion and ChIP-seq analysis, we found that TFAP2e depletion affected the expression of nine of the *hox*$^-$*;dlx2*$^+$ branch-specific genes, among them the early gene *mef2c*, and the late genes *dlx2, mmp14* and *vim*, and that TFAP2e directly bound four other cluster #11 genes: *c9, vim, mmp14 and mycn* (Fig. 5G, S9C). Direct regulation of *vim* and *mmp14* suggested that TFAP2e may be important for cranial NC EMT and migration. TFAP2e was previously reported to be important in NC induction (*49*). To test the later role of TFAP2e in NC migration, we devised an *in vivo* assay using low-level depletion of TFAP2e still allowing initial NC induction. Specifically, a pre-EMT NC explant microdissected from embryos co-injected with low-levels of TFAP2e MO, mRNA encoding an dexamethasone-inducible form of TFAP2e and a lineage tracer, was grafted into a wild-type control embryo at stage 17 (Fig. 5H). Morphant NC remained at the grafted site while wild-type cells efficiently populated the craniofacial areas (Fig. 5Hh,h'). Importantly, when TFAP2e was induced in morphant NC upon EMT stage, cell migration was restored and lineage-traced cells were found along NC cranial migration routes (Fig. 5Hh"). Together, these results validate branching analysis predictions and demonstrated that TFAP2e regulates expression of EMT effectors and cranial NC migration *in vivo*.

In conclusion, using computational approaches we have defined and analyzed three main bifurcation points in the premigratory NC dataset: from unbiased to vagal and cranial NC, from vagal NC to cardiac and ENSp fates, and from early cranial to either *rpe65*$^+$ or *dlx2*$^+$ cranial NC. For each branch we define specific gene programs, including early actors predicted to trigger specific states. Using ChIP-seq and MO-based small-RNAseq, we validate the link between numerous branch-specific genes and two early regulators, Pax3 and TFAP2e. We demonstrate that Pax3 displays early functions both in ENSp and in anterior cranial *rpe65*$^+$ NC branching. In parallel, TFAP2e activates branch-specific gene programs in *dlx2*$^+$ cranial NC as well as cell migration *in vivo*.

During gastrulation, the neural border zone emerges from overlapping ventral and dorsal programs, revealing multiple coexisting circuits for neural crest and placode lineage specification.

Neural border cells exhibit a gene signature regulated by main nodes of the ectoderm connectome.

Aiming to uncover the molecular mechanisms of cell fate decisions during NC induction at the neural-non neural ectoderm border zone, we analyzed a second dataset consisting of ectoderm cells for stages 11-13 (Fig. 1E). In this dataset we identified 10 cell clusters: *has1*$^+$ immature ectoderm at mid-gastrula stage 11 (cluster #0 - ec), two non-neural ectoderm populations (early *gata2*$^+$ cluster #2 - nne1 and later *tll2*$^+$ cluster #4 - nne2), *sox2*$^+$*, zic1*$^+$ neural ectoderm (cluster #1 - ne), *lhx2*$^+$ eye primordium (cluster #8 - eye), *sox9*$^+$*, c3*$^+$ NC progenitors (cluster #6 - nc), *pitx1*$^+$, *olfm4*$^+$ placode progenitors (cluster # 5 - pc), *neurog1*$^+$*, elavl3*$^+$ immature neurons (cluster #7 - neurons) and *zeb2*$^+$ neural plate (cluster #9 - np; Figs. 1E, 6A, B). Earlier work showed that NC and PC can develop from a common "neural border zone", defined as an ectodermal area located in-between *sox2*$^+$ NE and *epidermal keratin*$^+$ NNE and co-expressing *tfap2a, zic1* and *pax3* (Fig. S1) (*53*). The early developmental dynamics of this ectodermal area has not yet been described at the single-cell level, and it remains unknown if the cells in this area resemble adjacent progenitors or if they

exhibit a specific gene signature. On force-directed graph plot, this domain did not appear as an invididual cluster, rather as cells spread out between clusters 1, 2, 5 and 6 (Fig. 6A). PAGA graph analysis revealed that the *tfap2a*$^{+}$*, zic1*$^{+}$ cell group (nb, red cells) was equally similar to ne (#1) and nne (#2), and closer by 5.4 times to nc (#6) than to pc cluster (#5, Fig. 6A, C). We also observed a low density of cells at the levels of NB zone specifically between stage 11 and 12 (Fig. 6A). Because low density was not observed in neural or NNE areas, a stage-related sampling issue could be excluded. Rather this could be related to a faster transcriptional transition of the NB cells compared to NNE cells between stages 11 and 12/13 stages. This might suggest that early ectoderm cells go through NB state quickly before switching towards defined NC or PC states, resulting into fewer cells being captured in this transitional state upon sequencing. Alternatively, such clustering could be obtained if the NB zone ectoderm was highly heterogeneous and contained a mixture of NNE-like, NE-like and NB state cells.

We then sought to identify a detailed signature for the NB zone. Several genes were enriched as early as stage 11: *tfap2c, pax3, sox9, hes1, gmnn* and *myc* (Fig 1E, Fig. S1). Because *pax3* was previously found as one of the earliest NB zone specific genes (*2*), we examined the impact of Pax3 depletion on this NB zone signature *in vivo*. We found that expression of the other genes forming the NB signature, *sox9, axin2, zic3* and *zic1,* was decreased in Pax3 morphant NB while *lhx5.1,* highly expressed in earlier NE and NNE, was increased (Fig. 6C). These results consolidated Pax3 as a major switch for the early NB signature. In addition, Zic1 depletion also led to decreased expression of markers of the NB signature *zic3* and *gmmn* (Fig. 6D). In this case, *lhx5.s* was strongly decreased, contrarily to the effect of Pax3 depletion, indicating possible cooperative roles between Pax3 and Zic1 to balance a precise *lhx5* level compatible with neural border zone formation. Last, we defined other main nodes in the whole Ectoderm connectome (10085 gene connections) and found TFAP2a among the most significant ones (Table 2). We retrieved 682 direct targets of TFAP2a expressed in the NC dataset (Fig. S8), among the 1393 targets bound by TFAP2a in the whole embryo, including NB signature genes *pax3, sox9, myc and tfap2a* itself.

The NB zone contributes to NC and PC in parallel to convergent contributions from neural plate and non-neural ectoderm progenitors.

Based on the force-directed graph we found three possible developmental routes leading to NC and PC early states from stage 11 ectoderm cells: a) NE → NC; b) NB zone → PC and NC; c) NNE → PC (Fig. 7A, C-H). This was in line with both models currently proposed for NC and PC formation, namely the "neural border zone model" (route b) and the "neural vs non-neural" model (routes a & c) (Fig. 7A) (*16*, *53*, *54*). Interestingly, no direct route was found between nne1 and nc (Fig. 7D), or between ne and pc (Fig.7G), retrieving known biological features, such as the partial neuralization needed for NC induction or the close link between placodes and NNE (*17*, *18*). Because current tools cannot assess multiple branching simultaneously, we applied branching analysis for each potential developmental route in order to define and compare the gene programs underlying NC vs PC fate decisions along each route. For route (a), we found that branching towards NP from the NE state involved early genes *elav3 and sall2* and late genes *nkx6* and *tubb2b.* This was consistent with current knowledge on neural plate induction (*sall2, nkx6*) and primary neurogenesis (*elav3, tubb2b*), thus further validating the approach (Fig. 7C) (*55*). Route (a) branching towards NC involved early genes *zic1* and *foxd3* and late genes *c3, myc, sox8, sox9, pcdh8* and *snai2* (Fig. 7D). In comparison, NC cells emerging from the NB zone by route (b) started to express *c3* and *sox9* early, before bifurcation, while neural crest markers *foxd3*, *sox8, pcdh8, snail2* were enriched after splitting (Fig. 7E). Similarly, we explored gene programs for both routes of placodal development: from NB zone, route (b) showed early enrichment of *tcf7l1, hesx1* and late for *stmn1, pax6, pitx1/2* (Fig. 7F). PC development from NNE, i.e. route (c), exhibited early enrichment of placode specifiers *six1, otx2*, and late expression of placode markers *egflam, pax6, pitx1/2*, Fig. 7G). Last, the route (c) branching for non-neural ectoderm

formation confirmed known developmental dynamics with early enrichment for *gata2* and late for ectoderm stem cell marker *tp63* and epithelial cells *cldn1* (Fig. 7H) (*56*). This hierarchy of gene expression along the different branches thus sopens avenues to further elaborate each of the NC and PC GRNs.

Different gene programs can lead different progenitors towards a similar state.

Interestingly, according to the route studied, we found that (i) distinct genes were activated to obtain the same state, and that (ii) some genes were activated with different expression dynamics relative to different bifurcations. For example, during the NB→NC transition (route b, Fig. 7G), *sox9* and *c3* were activated early (before bifurcation) suggesting that they could play a part in the fate decision network from NB progenitors. In contrast, during the NE→NC gene program (Fig. 7D) *sox9* and *c3* were late genes while *foxd3* and *zic1* were expressed early. This observation suggested a new model of fate decisions in the developing ectoderm, where parallel and distinct genetic programs activated in distinct ectoderm progenitors may lead to a similar state.

We validated Zic1-related genetic regulations along route a: *in vivo* depletion of early-branch gene Zic1 increased expression of nc markers *sox8, foxd3* and *zic1* itself while it did not affect other NC late branch genes *sox9, c3, myc*, or *snai2* (Fig. 7B). Zic1 depletion also increased neuronal differentiation genes *tubb2b.l* and *tubb2b.s* in the np branch. This result supported a role for Zic1 in NP and NC development but also revealed complex interplay with Foxd3 (also early-branch) as Foxd3 enhanced expression may account for the activation of late-branch NC marker *sox8.*

Last, NB zone specific gene *pax3* was expressed prior to bifurcation in the route (b), NB→NC gene program, and controlled expression of late NC branch markers *sox9, sox8, foxd3, pcdh8* and *c3* (Fig. 7B). Moreover, Ectoderm connectome described NC genes connected to the rest of the network through Pax3 and Sox9 (Fig. 7I), suggesting that Sox9 might play a yet undescribed function downstream of Pax3 in NC induction and upstream of the other late NC branch markers. This was also in agreement with *sox9* being an early gene in the NB->NC branch. We tested the epistasis relationships between Pax3 and Sox9 in NC fate induction by combining Sox9 depletion or gain-of-function in the induced-neural crest assay (iNC is Pax3/Zic1-based NC induction from pluripotent ectoderm cells, Fig. 7J). *Snail2,* early marker of NC induction, starts to be expressed in the prospective NC from gastrula stage 12.5 both *in vivo* and in iNC, then is enhanced at neurula stage 14 (Fig. 7D, E, I). At both stages, co-activation of Sox9 strongly increased *snail2* expression, while Sox9 depletion reduced *snail2* activation (Fig. 7I, J). This result indicated that Sox9 is required for efficient NC induction by Pax3 and Zic1. Interestingly, when iNC explants were analyzed prior to the normal onset of *snail2* expression, at mid-gastrula stage 11/11.5, Sox9 activation drastically increased *snail2* expression, suggesting that Sox9 synergizes with Pax3 and Zic1 at the onset of NC induction (Fig. 7J).

In conclusion, we have defined a new transcriptional signature for the incompletely described Neural Border zone. We established a global Ectoderm connectome and validated experimentally NC-related nodes, in particular highlighting a novel function of Sox9 enhancing NC induction by Pax3 and Zic1. We characterized three different developmental routes branching towards NC and PC from the neural, neural border and non-neural ectoderm progenitors. We thus propose a model in which multiple co-existing paths can lead to common NC or PC states in gastrula-stage ectoderm.

Discussion

In this work, we exploit the unprecedented resolution of high-density single cell transcriptomes collected from an 8-stage developmental series to unravel the emergence of the neural crest lineage from the ectoderm during gastrulation followed by the diversification of neural crest progenitors during neurulation and upon EMT. Modeling gene transcription dynamics around each cell state allows inference of the underlying molecular networks. We selected several important nodes among those regulations for large-scale and *in vivo* experimental validation showing the good yet perfectible accuracy of machine learning-predicted networks (Fig. 8A-B). This study highlights the previously unknown temporal hierarchy of lineage decisions in neural crest development. Firstly, we characterize how the neural crest is activated either from a transient neural border state, or from a neural plate state at mid-gastrulation stage, and suggest a model that reconciles current debates upon the possible routes leading from immature ectoderm to neural crest and placodes (Fig. 8C). Secondly, we delineate the early and later neural crest trajectories that emerge during neurulation and define key regulators of branching, leading to eight transitional states and eight early migration states (Fig. 8D).

A reconciliatory "Model of Dual Convergence" describes the converging trajectories initiating neural crest and placode states.

The molecular signature of the neural border ectoderm has been overtly simple, with only Pax3 (in frog and fish) or Pax7 (in chick) as relatively specific markers for this domain during gastrulation and early neurulation stages (*9*, *14*). Here, we have characterized the neural border ectoderm state by two features: the lower level of expression of genes expressed by adjacent neural (dorsal) and non-neural (ventral) cells (*sox2*, *lhx2*, *sall2*, *gata2, ker19*) and the increased expression of a large gene list including *zic1, tfap2a/c, pax3*, *sox9, hes1, cmyc*. We find that this state seems more transient than other ectoderm states, suggesting that these fate decisions occur quickly. In frog embryos, the end of gastrulation is clearly defined by blastopore closure, and this allows more precise exploration of timing compared to organisms with simultaneous gastrulation and neurulation such as chick embryos. In frog, fate choices in the dorsal ectoderm happen during the second half of gastrulation (between stage 11 and 12.5). As the neural plate forms and the blastopore closes (stage 13), fate decisions are clearly established between neural, non-neural, placode and neural crest with robust molecular signatures (Fig. 6). Modeling neural crest emergence from the neural border cell state confirmed the central role for Pax3 and suggested novel epistatic relationships between Pax3 and Sox9 upstream of the definitive neural crest state, defined by persistent expression of *snail2*. With a temporal series of induced neural crest assay, Pax3 depletion and Pax3 ChIP, we validate the key role of Pax3 in the early NB/NC-GRN (Fig. 4) and the modeling-driven hypothesis that Sox9 displays an early function at the root of the NC-GRN (Fig. 7). Importantly, we propose a novel model for the pattern of fate decisions between the four main ectoderm fates, neural, non-neural, placodal, neural crest. Instead of contrasting “neural border” and “non-neural vs neural" hypotheses, we find that these routes are not exclusive and find trajectories supporting the emergence of neural crest from either the neural border or the nascent neural ectoderm on one hand, as well as two trajectories leading to placodes from either the neural border or the non-neural ectoderm. In each case, the gene programs underlying those alternative trajectories involve a subset of common genes and a few specific factors (Fig. 7). For example, specific expression of *tcf7l1* and *stmn1* is found in placodes arising from NB zone, compared to the NNE route (Fig. 7F, G). For neural crest, early *sox9* expression in the NB route contrasts with post-bifurcation expression in the NP route (Fig. GH7D, E). Thus, our SC transcriptome modeling reconciles and combines previously alternatives in a "Dual convergence Model" of neural crest and placode patterning, together with specific gene signatures for future functional exploration (Fig. 8C).

A combination of Omics and in vivo strategies validates large sets of gene regulations driving the dynamics of neural crest diversification.

The second outcome of our study is to define the temporal dynamics of trajectories that result into eight neural crest states present upon early migration stage along the cranial and vagal axial positions. The first key observation is the presence of a main population of NC unbiased towards any particular state, expressing markers of the immature neural crest cells, from which all the other trajectories emerge (Fig. 3). This unbiased cell trajectory is maintained during and after EMT suggesting that a very plastic, stem-like NC cell population emigrates and is subjected to the signals from the microenvironment prior to fate choices. The second critical observation is that, for the anterior part of the body axis considered here, trajectories do not emerge in a spatially linear sequence from anterior to posterior as previously anticipated in a model where NC would follow an anterior-posterior wave of maturation. Two early trajectories arise from both the anterior (progenitors of posterior cranial NC - cluster #15) and the posterior-most positions (minor vagal trajectory progenitors, cluster #3) at neural plate stage (stages 13-14) prior to neural fold elevation. This is followed at mid-neurula stage (stage 15-16) by the emergence of the three other main cranial and vagal trajectories leading to cranial clusters #10 and #11, and to vagal NC clusters #12 and #13. Together with the maintenance of an immature stem-like cell population from induction to emigration, this sequence of trajectory determination suggests that the main cue controlling the temporal dynamics of states hierarchy in the cranial and vagal NC-GRN is not a function of the time elapsed since NC cell induction, or correlated to Hox gene positional information, but rather would involve response to external signals. This hypothesis is supported by the strong retinoic-acid response signature which defines the posterior cranial lineage from neural plate to emigration stages, and maintains this trajectory distinct from the unbiased NC population.

Our temporal analysis highlights three important points deepening our understanding of NC biology. Firstly, there have been long standing debates about the timing of NC fate decisions, prior or after EMT from the neural tube, in a variety of animal models (*57*). Importantly, we did not detect distinctive expression of predictive fate markers before EMT (e.g. for neuronal, glial skeletogenic or melanocyte fates). This suggested that, if some NC progenitors were biased towards a given fate prior to EMT, they did not exhibit a detectable signature in our dataset. However, our observations are in agreement with several lineage tracing studies showing the high multipotency of most NC cells when marked prior to EMT (*58*). The first differentiation markers are found after emigration, as we detected myosin-like expression in a small subset of cells suggesting the emergence of previously poorly described NC-derived myofibroblasts shortly after EMT (Fig. 3E). It also supports that our dataset is sensitive enough to detect other fate-specific markers if they were expressed at the end of neurulation. Secondly, our data supports the early diversification into several distinct cell states prior, during and after EMT, contrasting with recent suggestion that upon EMT the NC progenitors would regroup into a single common multipotent state (*13*). The high cell content of our dataset proves otherwise, suggesting that this previous observation made on a smaller subset of cranial NC did not fully capture the diversity of pre-migratory NC states. Lastly, temporal trajectory analysis unravels the branch-specific dynamics of gene expression underlying bifurcations and state diversification. For each bifurcation, we provide a list of key genes likely to control branching choices (Figs. 5,7). We further validate these predictions in several instances, by experimental modulation of pivotal transcription factors function in the premigratory neural crest (Pax3, Zic1, TFAP2a, TFAP2e), followed by *in vivo* or deep sequencing analysis. This strategy proves versatile and powerful to validate the predictions of SC transcriptomics on a large scale.

In sum, our study provides a comprehensive view of the hierarchy of molecular decisions driving the cranial and vagal neural crest gene regulatory network from induction at the neural border to early migration, with unprecedented resolution and deep learning-aided experimental validation. We propose a new "Dual Convergence Model" for neural crest and placode lineage emergence, and provide a detailed roadmap of the main molecular events in

the premigratory and early migrating NC-GRN. Using a dedicated interactive network visualization interface, any gene of interest can be queried. Moreover, the detailed view of lineage formation provided here will prove an essential reference for monitoring induction of neural crest derivatives, for example from patient-derived induced pluripotent stem cells, when reliable specification protocols preferably recapitulate the steps of embryonic development.

Materials and Methods

Experimental Design

Single cell transcriptomes from developing frog embryos were scrutinized for neural crest progenitor development using machine-learning tools to infer the gene regulatory network connectome and the gene programs underlying branching of fates. These predictions were largely validated *in vivo* using micro-manipulations in *X. laevis* embryos followed by RNA-seq or ChIPseq.

Single cell sequencing

No new materials were collected for this study. Instead, we re-sequenced the RNA libraries for developmental stages NF11 to NF22 (*59*) used in (*17*). Please refer to the methods therein for staging, embryo collection, dissociation, cell collection, barcoding (inDrop v2 and v3) and library preparation methods. For re-sequencing, we used two flow cells (two lanes each) of NovaSeq S2 at 100 cycles setting generating a total of 12 billion reads. All datasets are deposited under NCBI Gene Expression Omnibus number GSE198494.

Reference genome and gene symbol assignments

For bioinformatics analysis of SC dataset, we used the *X.tropicalis* v.10 genome assembly, gene models v. 10.7. Specifically, we used the file Xentr10-Gene-Sym-HUMAN-BLOSUM45.txt downloaded from Xenbase on Nov 5th, 2021. Thousands of genes in that transcriptome version lack interpretable gene symbols, though in many cases an unambiguous protein identity can be identified by sequence homology. To fill the holes in gene symbol assignments we assigned protein gene symbols to each transcript using a modified reciprocal best HMMER hit approach (*60*) based on a target reference set of curated human proteins.

scRNA-seq reads processing

Compared to (*17*), we selected a different aligner and scRNA pipeline since Bowtie (*61*), which was used in the InDrops pipeline (*62*), was not designed to align transcripts to the genome, and therefore is not splice-aware. A splice-aware algorithm does not align RNA-seq reads to introns, and identifies possible downstream exons trying to align to those instead. Moreover, using Bowtie for aligning reads to a transcriptome raises questions about choosing the correct transcript. Therefore, we chose STAR, since it is one of the best RNA-seq aligners and outperforms other aligners in terms of correctly and incorrectly aligned reads (*63*). Also, it is fast and there is no need to do preprocessing by removing bad quality bases or adapters as STAR does that internally (*64*). We used the DropEst pipeline (*65*). Recent benchmarking shows that DropEst exceeds other options in terms of sensitivity and efficiency (running time and memory use) (*66*). As a result, for v3 we used Indrops demultiplexing and soft filtering, then we generated tagged files similar to dropTag without considering reads base quality for barcodes, followed by alignment and quantification with STAR (outFilterMatchNminOverLread 0.44 --outFilterScoreMinOverLread 0.44) and dropEst using X.trop v10. After filtration by counts and genes numbers (>200 genes; >300 counts), we gathered a dataset of 177250 cells. In the cells of interest (Ectoderm and NC cells), mean counts number was 1778, and mean gene number was 1035.

scRNA-seq postprocessing

To process scRNA data we used Scanpy (*25*), a comprehensive scRNA pipeline that is functionally similar to Seurat (*67*). Firstly, we calculated the percentage of mitochondrial

(MT) and ribosomal (RB) genes per cell,by manually calculating the fraction of mitochondrial reads and ribosomal reads. As high MT proportions indicate poor quality cells (*68*), presumably due to loss of cytoplasmic RNA from perforated cells, we removed cells with a high percentage of MT/RB transcripts. Then, we removed gene sets which might affect the normalization step. These include foreign tissue contaminants, heatshock, ribosomal, clock and hemoglobin genes. For normalization, we excluded the expression of genes if their expression was more than 3 percent of the total expression of the cell, because it could greatly affect the resulting normalized values for all other genes (*69*). Next, we assessed the cell cycle dynamics. The algorithm calculates the difference between the mean of the given list of cell cycle genes and the mean of the reference genes. To build such a reference, we randomly selected a set of genes that matched the distribution of the expression in the list. This way we got S phase, G2M phase scores for each cell. We did not regress out cell cycle effect because it had no significant influence. For normalization, we used scanpy function *scanpy.pp.normilize_total* without highly expressing genes and target_sum=10^4.

Clustering and NC cells selection

For each stage, we performed independent standard dimensionality reduction with PCA, computing a neighborhood graph (n_pcs selected based on the amount of variance explained by each PC, n_neighbors selected manually) and UMAP (*70*). For clustering, we used the Leiden algorithm (*24*). For each cluster, we defined cluster-specific genes with differential expression analysis (scanpy t-test_overestim_var) and selected only clusters which were the most similar to NC cells using NC signatures from (*17*).

NC classifier

First, we generated a dataset by labeling cells as NC based on the previous differential expression analysis between clusters (*17*). For feature selection, we trained the LightGBM model (*20*) on the whole embryo dataset of 177250 cells, retrieved the top 2000 important features and used it for re-training the model (default setting with n_estimators=500). The resulting model detected NC cells in the test dataset from the *Xenopus tropicalis* dataset with accuracy 0.99 and F1 score 0.90. Only the trained dataset sample was used to get the top important features and retrain the model on the top 2000 features. To test the model robustness, we validated the NC classifier in the Zebrafish scRNA-seq dataset (*21*). We used a sigmoid function to smoothen the technical batch effect between the datasets. Genes that were not found in the Zebrafish dataset were replaced with NaN values (728 from top 2000 important genes were not found in the Zebrafish dataset). Finally, our model predicted NC cells in the Zebrafish dataset with AUC score 0.95 and F1 score 0.66 (in comparison, the random model with strategy="stratified" (https://scikit-learn.org/stable/modules/generated/sklearn.dummy.DummyClassifier.html) applied on the imbalanced Wagner dataset has F1 score=0.05).

GRN generation

To predict the NC-GRN, we used GRNBoost2 (*43*), one of the best GRN predictors according to recent benchmarking (*42*). Through this algorithm, for each gene in the cell-gene matrix, a tree-based regression model is built to predict gene expression using the expression of TFs. Each gene-specific model produces a partial GRN with regulatory associations from the most predictive TFs for the gene. Then, all regulatory associations are pooled and ranked by importance to complete the GRN. The *Xenopus* TF list (1417 TFs) was taken from *Xenopus tropicalis* TF catalog (*45*). We analyzed the resulting network of TFs and their targets using the networkx package and identified the most important nodes by calculating betweenness and degree centralities with betweenness_centrality, degree_centrality network functions.

Principal graph generation

The tree analysis was carried out using the scFates package (*50*), based on ElPiGraph using the concept of elastic energy and a gradient descent-like optimization of the graph topology (*50*). However, this approach is too sensitive to build the principal graph for the whole NC dataset. Therefore, to generate the main tree, we used the PAGA algorithm (*25*). This revealed cluster-cluster relationships including the early stages where the strongest connectivity was observed. Further we used ElPiGraph to study specific branches and bifurcation points.

Branching analysis

Using ScFates we defined features significantly changing along the tree, and then using pseudotime values and differential expression analysis, determined early and late branch-specific features. For each bifurcation point of interest, we selected a set of cells related to the clusters involved in the bifurcation. The selection of parameters for building the principal tree for each point of the bifurcation was carried out using brute force approach.

Chromatin immunoprecipitation sequencing (ChIPseq)

Chromatin immunoprecipitation was performed according to (*71*). Embryos were injected in both blastomeres at the two-cell stage with tracing amounts (75 pg) of mRNA encoding either Pax3-FLAG-HA, or TFAP2a-FLAG or TFAP2e-FLAG. Injected embryos were collected at mid-neurula stage 14 (Pax3 and TFAP2a, 100 *X. laevis* embryos/condition) or at NC early migratory stage 19 (TFAP2e, 100 *X. tropicalis* embryos/condition). IP efficiency was tested on *snai2* promoter (Table S9). After sequencing, 100 bp single-end reads were aligned to *X. laevis* genome version 9.2 or *X. tropicalis* v10.0 using bowtie2. Peaks were called using MACS2. For Pax3 and TFAP2a, we selected peaks common in three replicates, for TFAP2e we used stricter MACS2 score cutoff=500. Target genes were searched with bedtools (window size = 10kb).

In vivo experiments: Xenopus laevis injections, microdissections, grafting and small RNA-seq

In vivo injections, NB/NC dissections and grafting were done as previously (*2*, *72*) using *X. laevis* embryos. For knockdown experiments, previously validated antisense morpholino oligonucleotides (MO) were used to deplete *pax3, zic1,* and *tfap2e* transcripts (GeneTools). Pax3 or Zic1 MO (20ng) (*9*, *73*) or *tfap2e* MO (20ng) (*49*). Depletion efficiency was verified using in situ hybridization on sibling embryos to verify reduction of *snai2* expression (not shown). One Pax3 morphant anterior NB explant (stage 14) or one TFAP2e-morphant NC explant (stage 17) were dissected from the injected side, in triplicate. After RNA extraction and cDNA library preparation, each individual explant was sequenced (small RNA-seq). The resulting 100 bp paired-end sequencing reads were aligned to the *X. laevis* genome version 9.2 using STAR and the count reads were analyzed using String Tie. Differentially expressed genes were selected considering log2FC and expression difference in absolute values (abs. diff. >=100 and <=500: log2FC>1.5 or log2FC<-1.5; abs. diff >=500 and <=1000: log2FC>1 or log2FC<-1; abs. diff >=1000 and <=3000: log2FC>0.5 or log2FC<-0.5; abs.diff.>3000: log2FC>0.33 or log2FC<-0.33)

iNC assay, RNA quantification and RT-qPCR

The induced neural crest assay (iNC) used co-activation of dexamethasone-inducible Pax3-GR and Zic1-GR at gastrula initiation stage 10.5, in pluripotent blastula ectoderm (animal caps dissected at blastula stage 9) (*29*, *74*). This was combined with Sox9 depletion (40 ng of *sox9* MO) (*75*), or gain-of-function (300 pg *sox9* mRNA). At the desired stage, explants were harvested and processed for RTqPCR as in (*18*). Primers listes in Table S9.

Whole-mount in situ hybridization (ISH)

Whole-mount *in situ* hybridization followed a protocol optimized for superficial structures (*76*). Embryos were imaged using a Lumar V12 Binocular microscope equipped with bright field and color cameras (Zeiss).

References

1. B. F. Eames, D. M. Medeiros, I. Adameyko, *Evolving Neural Crest Cells* (CRC Press, 2020).

2. J.-L. Plouhinec, S. Medina-Ruiz, C. Borday, E. Bernard, J.-P. Vert, M. B. Eisen, R. M. Harland, A. H. Monsoro-Burq, A molecular atlas of the developing ectoderm defines neural, neural crest, placode, and nonneural progenitor identity in vertebrates. *PLOS Biology*. **15**, e2004045 (2017).

3. B. Steventon, R. Mayor, Early neural crest induction requires an initial inhibition of Wnt signals. *Dev Biol*. **365**, 196–207 (2012).

4. A. Streit, C. D. Stern, Establishment and maintenance of the border of the neural plate in the chick: involvement of FGF and BMP activity. *Mechanisms of Development*. **82**, 51–66 (1999).

5. D. Bhattacharya, A. P. Azambuja, M. Simoes-Costa, Metabolic Reprogramming Promotes Neural Crest Migration via Yap/Tead Signaling. *Dev Cell*. **53**, 199-211.e6 (2020).

6. A. L. Figueiredo, F. Maczkowiak, C. Borday, P. Pla, M. Sittewelle, C. Pegoraro, A. H. Monsoro-Burq, *Development*, in press, doi:10.1242/dev.157644.

7. I. T. C. Ling, T. Sauka-Spengler, Early chromatin shaping predetermines multipotent vagal neural crest into neural, neuronal and mesenchymal lineages. *Nat Cell Biol*. **21**, 1504–1517 (2019).

8. W. Tang, Y. Li, A. Li, M. E. Bronner, Clonal analysis and dynamic imaging identify multipotency of individual Gallus gallus caudal hindbrain neural crest cells toward cardiac and enteric fates. *Nat Commun*. **12**, 1894 (2021).

9. A.-H. Monsoro-Burq, E. Wang, R. Harland, Msx1 and Pax3 cooperate to mediate FGF8 and WNT signals during Xenopus neural crest induction. *Dev Cell*. **8**, 167–178 (2005).

10. M. Simoes-Costa, M. E. Bronner, Reprogramming of avian neural crest axial identity and cell fate. *Science*. **352**, 1570–1573 (2016).

11. L. Medina-Cuadra, A. H. Monsoro-Burq, Xenopus, an emerging model for studying pathologies of the neural crest. *Curr Top Dev Biol*. **145**, 313–348 (2021).

12. K. B. Artinger, A. H. Monsoro-Burq, Neural crest multipotency and specification: power and limits of single cell transcriptomic approaches. *Fac Rev*. **10**, 38 (2021).

13. A. Zalc, R. Sinha, G. S. Gulati, D. J. Wesche, P. Daszczuk, T. Swigut, I. L. Weissman, J. Wysocka, Reactivation of the pluripotency program precedes formation of the cranial neural crest. *Science*. **371**, eabb4776 (2021).

14. M. L. Basch, M. Bronner-Fraser, M. I. García-Castro, Specification of the neural crest occurs during gastrulation and requires Pax7. *Nature*. **441**, 218–222 (2006).

15. A. K. Groves, C. LaBonne, Setting appropriate boundaries: Fate, patterning and competence at the neural plate border. *Dev Biol*. **389**, 2–12 (2014).

16. S. K. Maharana, G. Schlosser, A gene regulatory network underlying the formation of pre-placodal ectoderm in Xenopus laevis. *BMC Biol*. **16**, 79 (2018).

17. J. A. Briggs, C. Weinreb, D. E. Wagner, S. Megason, L. Peshkin, M. W. Kirschner, A. M. Klein, The dynamics of gene expression in vertebrate embryogenesis at single-cell resolution. *Science*. **360**, eaar5780 (2018).

18. M. Alkobtawi, P. Pla, A. H. Monsoro-Burq, BMP signaling is enhanced intracellularly by FHL3 controlling WNT-dependent spatiotemporal emergence of the neural crest. *Cell Reports*. **35**, 109289 (2021).

19. N. de Crozé, F. Maczkowiak, A. H. Monsoro-Burq, Reiterative AP2a activity controls sequential steps in the neural crest gene regulatory network. *Proc Natl Acad Sci U S A*. **108**, 155–160 (2011).

20. G. Ke, Q. Meng, T. Finley, T. Wang, W. Chen, W. Ma, Q. Ye, T.-Y. Liu, in *Advances in Neural Information Processing Systems* (Curran Associates, Inc., 2017; https://proceedings.neurips.cc/paper/2017/hash/6449f44a102fde848669bdd9eb6b76fa-Abstract.html), vol. 30.

21. D. E. Wagner, C. Weinreb, Z. M. Collins, J. A. Briggs, S. G. Megason, A. M. Klein, Single-cell mapping of gene expression landscapes and lineage in the zebrafish embryo. *Science*. **360**, 981–987 (2018).

22. C. Pegoraro, A. H. Monsoro-Burq, Signaling and transcriptional regulation in neural crest specification and migration: lessons from xenopus embryos. *Wiley Interdiscip Rev Dev Biol*. **2**, 247–259 (2013).

23. A. Thawani, A. K. Groves, Building the Border: Development of the Chordate Neural Plate Border Region and Its Derivatives. *Front Physiol*. **11**, 608880 (2020).

24. V. A. Traag, L. Waltman, N. J. van Eck, From Louvain to Leiden: guaranteeing well-connected communities. *Sci Rep*. **9**, 5233 (2019).

25. F. A. Wolf, P. Angerer, F. J. Theis, SCANPY: large-scale single-cell gene expression data analysis. *Genome Biology*. **19**, 15 (2018).

26. S. Tani-Matsuhana, K. Inoue, Identification of regulatory elements for MafB expression in the cardiac neural crest. *Cells Dev*. **167**, 203725 (2021).

27. S. E. Akbareian, N. Nagy, C. E. Steiger, J. D. Mably, S. A. Miller, R. Hotta, D. Molnar, A. M. Goldstein, Enteric neural crest-derived cells promote their migration by modifying their microenvironment through tenascin-C production. *Developmental Biology*. **382**, 446–456 (2013).

28. J. England, S. Loughna, Heavy and light roles: myosin in the morphogenesis of the heart. *Cell Mol Life Sci*. **70**, 1221–1239 (2013).

29. C. Milet, F. Maczkowiak, D. D. Roche, A. H. Monsoro-Burq, Pax3 and Zic1 drive induction and differentiation of multipotent, migratory, and functional neural crest in Xenopus embryos. *Proc Natl Acad Sci U S A*. **110**, 5528–5533 (2013).

30. E. Nitzan, S. Krispin, E. R. Pfaltzgraff, A. Klar, P. A. Labosky, C. Kalcheim, A dynamic code of dorsal neural tube genes regulates the segregation between neurogenic and melanogenic neural crest cells. *Development*. **140**, 2269–2279 (2013).

31. J. A. Morrison, R. McLennan, J. M. Teddy, A. R. Scott, J. C. Kasemeier-Kulesa, M. M. Gogol, P. M. Kulesa, Single-cell reconstruction with spatial context of migrating neural crest cells and their microenvironments during vertebrate head and neck formation. *Development*. **148**, dev199468 (2021).

32. P. L. Martínez-Morales, R. Diez del Corral, I. Olivera-Martínez, A. C. Quiroga, R. M. Das, J. A. Barbas, K. G. Storey, A. V. Morales, FGF and retinoic acid activity gradients control the timing of neural crest cell emigration in the trunk. *J Cell Biol*. **194**, 489–503 (2011).

33. R. A. S. Kjolby, R. M. Harland, Genome-wide identification of Wnt/β-catenin transcriptional targets during Xenopus gastrulation. *Dev Biol*. **426**, 165–175 (2017).

34. R. K. T. Kam, W. Shi, S. O. Chan, Y. Chen, G. Xu, C. B.-S. Lau, K. P. Fung, W. Y. Chan, H. Zhao, Dhrs3 protein attenuates retinoic acid signaling and is required for early embryonic patterning. *J Biol Chem*. **288**, 31477–31487 (2013).

35. A. J. Burns, P. J. Pasricha, H. M. Young, Enteric neural crest-derived cells and neural stem cells: biology and therapeutic potential. *Neurogastroenterol Motil*. **16 Suppl 1**, 3–7 (2004).

36. A. Collazo, M. Bronner-Fraser, S. E. Fraser, Vital dye labelling of Xenopus laevis trunk neural crest reveals multipotency and novel pathways of migration. *Development*. **118**, 363–376 (1993).

37. V. Sasselli, V. Pachnis, A. J. Burns, The enteric nervous system. *Dev Biol*. **366**, 64–73 (2012).

38. N. Nagy, T. Kovacs, R. Stavely, V. Halasy, A. Soos, E. Szocs, R. Hotta, H. Graham, A. M. Goldstein, *Development*, in press, doi:10.1242/dev.199825.

39. P. M. Helbling, C. T. Tran, A. W. Brändli, Requirement for EphA receptor signaling in the segregation of Xenopus third and fourth arch neural crest cells. *Mech Dev*. **78**, 63–79 (1998).

40. M. Addison, Q. Xu, J. Cayuso, D. G. Wilkinson, Cell Identity Switching Regulated by Retinoic Acid Signaling Maintains Homogeneous Segments in the Hindbrain. *Dev Cell*. **45**, 606-620.e3 (2018).

41. R. Lumb, S. Wiszniak, S. Kabbara, M. Scherer, N. Harvey, Q. Schwarz, Neuropilins define distinct populations of neural crest cells. *Neural Dev*. **9**, 24 (2014).

42. A. Pratapa, A. P. Jalihal, J. N. Law, A. Bharadwaj, T. M. Murali, Benchmarking algorithms for gene regulatory network inference from single-cell transcriptomic data. *Nat Methods*. **17**, 147–154 (2020).

43. T. Moerman, S. Aibar Santos, C. Bravo González-Blas, J. Simm, Y. Moreau, J. Aerts, S. Aerts, GRNBoost2 and Arboreto: efficient and scalable inference of gene regulatory networks. *Bioinformatics*. **35**, 2159–2161 (2019).

44. C. Niehrs, N. Pollet, Synexpression groups in eukaryotes. *Nature*. **402**, 483–487 (1999).

45. I. L. Blitz, K. D. Paraiso, I. Patrushev, W. T. Y. Chiu, K. W. Y. Cho, M. J. Gilchrist, A catalog of Xenopus tropicalis transcription factors and their regional expression in the early gastrula stage embryo. *Dev Biol*. **426**, 409–417 (2017).

46. J.-L. Plouhinec, D. D. Roche, C. Pegoraro, A.-L. Figueiredo, F. Maczkowiak, L. J. Brunet, C. Milet, J.-P. Vert, N. Pollet, R. M. Harland, A. H. Monsoro-Burq, Pax3 and Zic1 trigger the early neural crest gene regulatory network by the direct activation of multiple key neural crest specifiers. *Dev Biol*. **386**, 461–472 (2014).

47. M. Uehara, K. Yashiro, S. Mamiya, J. Nishino, P. Chambon, P. Dolle, Y. Sakai, CYP26A1 and CYP26C1 cooperatively regulate anterior-posterior patterning of the developing brain and the production of migratory cranial neural crest cells in the mouse. *Dev Biol*. **302**, 399–411 (2007).

48. M. Xu, Y. Li, J. Du, H. Lin, S. Cao, Z. Mao, R. Wu, M. Liu, Y. Liu, Q. Yin, PAX3 Promotes Cell Migration and CXCR4 Gene Expression in Neural Crest Cells. *J Mol Neurosci*. **64**, 1–8 (2018).

49. C.-S. Hong, A. Devotta, Y.-H. Lee, B.-Y. Park, J.-P. Saint-Jeannet, Transcription factor AP2 epsilon (Tfap2e) regulates neural crest specification in Xenopus. *Dev Neurobiol*. **74**, 894–906 (2014).

50. L. Albergante, E. Mirkes, J. Bac, H. Chen, A. Martin, L. Faure, E. Barillot, L. Pinello, A. Gorban, A. Zinovyev, Robust and Scalable Learning of Complex Intrinsic Dataset Geometry via ElPiGraph. *Entropy*. **22**, 296 (2020).

51. N. Le Douarin, C. Kalcheim, *The Neural Crest* (Cambridge University Press, Cambridge, ed. 2, 1999; https://www.cambridge.org/core/books/neural-crest/CC1993A22EDB67E40992CC2FD3771536), *Developmental and Cell Biology Series*.

52. S. G. Gonzalez Malagon, K. J. Liu, ALK and GSK3: Shared Features of Neuroblastoma and Neural Crest Cells. *J Exp Neurosci*. **12**, 1179069518792499 (2018).

53. S. Seal, A. H. Monsoro-Burq, Insights Into the Early Gene Regulatory Network Controlling Neural Crest and Placode Fate Choices at the Neural Border. *Front Physiol*. **11**, 608812 (2020).

54. D. Roellig, J. Tan-Cabugao, S. Esaian, M. E. Bronner, Dynamic transcriptional signature and cell fate analysis reveals plasticity of individual neural plate border cells. *Elife*. **6**, e21620 (2017).

55. C. R. T. Exner, A. Y. Kim, S. M. Mardjuki, R. M. Harland, sall1 and sall4 repress pou5f3 family expression to allow neural patterning, differentiation, and morphogenesis in Xenopus laevis. *Developmental Biology*. **425**, 33–43 (2017).

56. M. Haas, J. L. Gómez Vázquez, D. I. Sun, H. T. Tran, M. Brislinger, A. Tasca, O. Shomroni, K. Vleminckx, P. Walentek, ΔN-Tp63 Mediates Wnt/β-Catenin-Induced Inhibition of Differentiation in Basal Stem Cells of Mucociliary Epithelia. *Cell Rep*. **28**, 3338-3352.e6 (2019).

57. C. Kalcheim, D. Kumar, Cell fate decisions during neural crest ontogeny. *Int J Dev Biol*. **61**, 195–203 (2017).

58. A. Baggiolini, S. Varum, J. M. Mateos, D. Bettosini, N. John, M. Bonalli, U. Ziegler, L. Dimou, H. Clevers, R. Furrer, L. Sommer, Premigratory and migratory neural crest cells are multipotent in vivo. *Cell Stem Cell*. **16**, 314–322 (2015).

59. J. Faber, P. D. Nieuwkoop, *Normal Table of Xenopus Laevis (Daudin): A Systematical & Chronological Survey of the Development from the Fertilized Egg till the End of Metamorphosis* (Garland Science, 2020).

60. V. Savova, E. J. Pearl, E. Boke, A. Nag, I. Adzhubei, M. E. Horb, L. Peshkin, Transcriptomic insights into genetic diversity of protein-coding genes in X. laevis. *Dev Biol*. **424**, 181–188 (2017).

61. B. Langmead, C. Trapnell, M. Pop, S. L. Salzberg, Ultrafast and memory-efficient alignment of short DNA sequences to the human genome. *Genome Biology*. **10**, R25 (2009).

62. A. M. Klein, L. Mazutis, I. Akartuna, N. Tallapragada, A. Veres, V. Li, L. Peshkin, D. A. Weitz, M. W. Kirschner, Droplet barcoding for single cell transcriptomics applied to embryonic stem cells. *Cell*. **161**, 1187–1201 (2015).

63. G. Baruzzo, K. E. Hayer, E. J. Kim, B. Di Camillo, G. A. FitzGerald, G. R. Grant, Simulation-based comprehensive benchmarking of RNA-seq aligners. *Nat Methods*. **14**, 135–139 (2017).

64. A. Dobin, C. A. Davis, F. Schlesinger, J. Drenkow, C. Zaleski, S. Jha, P. Batut, M. Chaisson, T. R. Gingeras, STAR: ultrafast universal RNA-seq aligner. *Bioinformatics*. **29**, 15–21 (2013).

65. V. Petukhov, J. Guo, N. Baryawno, N. Severe, D. T. Scadden, M. G. Samsonova, P. V. Kharchenko, dropEst: pipeline for accurate estimation of molecular counts in droplet-based single-cell RNA-seq experiments. *Genome Biology*. **19**, 78 (2018).

66. M. Gao, M. Ling, X. Tang, S. Wang, X. Xiao, Y. Qiao, W. Yang, R. Yu, Comparison of high-throughput single-cell RNA sequencing data processing pipelines. *Briefings in Bioinformatics*. **22**, bbaa116 (2021).

67. T. Stuart, A. Butler, P. Hoffman, C. Hafemeister, E. Papalexi, W. M. Mauck, Y. Hao, M. Stoeckius, P. Smibert, R. Satija, Comprehensive Integration of Single-Cell Data. *Cell*. **177**, 1888-1902.e21 (2019).

68. A. T. L. Lun, D. J. McCarthy, J. C. Marioni, A step-by-step workflow for low-level analysis of single-cell RNA-seq data with Bioconductor. *F1000Res*. **5**, 2122 (2016).

69. C. Weinreb, S. Wolock, B. K. Tusi, M. Socolovsky, A. M. Klein, Fundamental limits on dynamic inference from single-cell snapshots. *PNAS*. **115**, E2467–E2476 (2018).

70. M. Jacomy, T. Venturini, S. Heymann, M. Bastian, ForceAtlas2, a Continuous Graph Layout Algorithm for Handy Network Visualization Designed for the Gephi Software. *PLOS ONE*. **9**, e98679 (2014).

71. A. E. Wills, R. Gupta, E. Chuong, J. C. Baker, Chromatin immunoprecipitation and deep sequencing in Xenopus tropicalis and Xenopus laevis. *Methods*. **66**, 410–421 (2014).

72. C. Milet, A. H. Monsoro-Burq, Dissection of Xenopus laevis neural crest for in vitro explant culture or in vivo transplantation. *J Vis Exp* (2014), doi:10.3791/51118.

73. T. Sato, N. Sasai, Y. Sasai, Neural crest determination by co-activation of Pax3 and Zic1 genes in Xenopus ectoderm. *Development*. **132**, 2355–2363 (2005).

74. C.-S. Hong, J.-P. Saint-Jeannet, The Activity of Pax3 and Zic1 Regulates Three Distinct Cell Fates at the Neural Plate Border. *MBoC*. **18**, 2192–2202 (2007).

75. R. F. Spokony, Y. Aoki, N. Saint-Germain, E. Magner-Fink, J.-P. Saint-Jeannet, The transcription factor Sox9 is required for cranial neural crest development in Xenopus. *Development*. **129**, 421–432 (2002).

76. Monsoro-Burq AH. A rapid protocol for whole-mount in situ hybridization on Xenopus embryos. CSH Protoc. 2007 Aug 1;2007:pdb.prot4809. doi: 10.1101/pdb.prot4809. PubMed PMID: 21357147.

Supplementary references

77. M. Nichane, X. Ren, J. Souopgui, E. J. Bellefroid, Hairy2 functions through both DNA-binding and non DNA-binding mechanisms at the neural plate border in Xenopus. *Developmental Biology*. **322**, 368–380 (2008).

Acknowledgements

The authors are grateful to Drs. Andrej Zinoviev, Gerhard Schlosser, Igor Adameyko and Thomas Walter for insightful scientific discussions and comments on the manuscript. We thank C. Lantoine for animal husbandry, Q. Thuillier for technical assistance. We thank J. Briggs for help in single cell sequencing. We thank J.L. Plouhinec for initial analysis of small RNAseq. High-throughput sequencing, except for single cell sequencing, has been performed by the ICGex NGS platform of the Institut Curie supported by the grants ANR-10-EQPX-03 (Equipex) and ANR-10-INBS-09-08 (France Génomique Consortium) from the Agence Nationale de la Recherche ("Investissements d'Avenir" program), by the Canceropole Ile-de-France and by the SiRIC-Curie program -SiRIC Grant « INCa-DGOS-4654 ».

Funding:
This project receives funding from
European Union's Horizon 2020 research and innovation programme under Marie Skłodowska-Curie grant agreement No 860635, NEUcrest ITN (AHMB)
Agence Nationale pour la Recherche (ANR-15-CE13-0012-01; AHMB)
Agence Nationale pour la Recherche ANR-21-CE13-0028; AHMB)
Institut Universitaire de France (AHMB)
National Institutes of Health NICHD award R01HD073104 (LP)
National Institutes of Health NIH R01 GM42341 (RMH)
National Institutes of Health NIH R35GM127069 (RMH)

Author contributions:
Conceptualization: AK, SS, LP, AHMB
Methodology: AK, MA, SS, VK, SMR, HA, LP, AHMB
Investigation: AK, MA, SS, VK, HA, LP, AHMB
Visualization: AK, MA, SS, VK, AHMB
Supervision: LP, RMH, AHMB
Writing—original draft: AK, SS, AHMB
Writing—review & editing: AK, SS, RMH, AHMB

Competing interests: Authors declare that they have no competing interests.

Data and materials availability: All data are available in the main text or the supplementary materials. Accession numbers to the datasets, together with their description are under NCBI Gene Expression Omnibus # GSE198494.

Figures and Tables

1202

Kotov et al., Figure 1

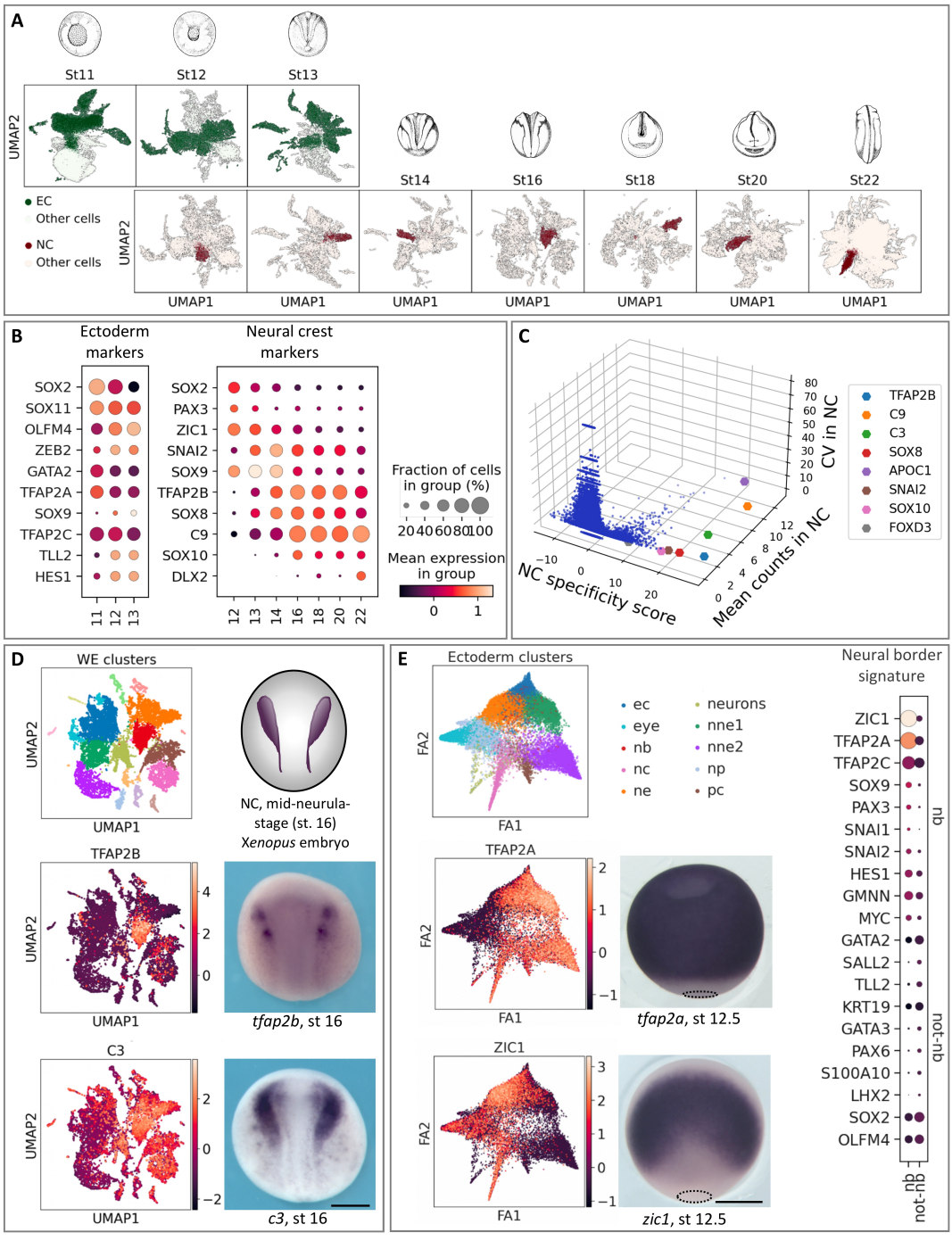

Fig. 1. Cell selection for neural crest, ectoderm and neural border. (A) Ectoderm (EC, stages 11-13, green) and NC cells (stages 12-22, brown) were selected from a whole embryo SC transcriptome dataset of 177250 cells. (**B)** Dotplots for well-referenced gene expressions used to identify EC and NC at each stage. Dot size represents the number of cells expressing the gene, color represents the average expression level. (**C)** 3D scatter-plot of NC score specificity (z-scores), mean gene expression levels and coefficient of variation (CV) in NC cells, defining a few highly expressed pan-NC genes during neurulation. (**D)** Mid-neurula stage 16 whole embryo UMAP and ISH show expression of *tfap2b,* specifically in NC cells, and of *c3*, in NC cells and also neural and non neural ectoderm. (**E)** NB signature was defined by differential expression analysis of cells highly co-expressing *tfap2a* and *zic1* (nb, UMAP and ISH) compared to the other ectoderm cells (not-nb): in addition to *tfap2a* and *zic1*, the genes enriched in the NB zone are *sox9, pax3, snai1/2, hes1, gmnn and myc*. Scale bar, 500 μm.

1218

Kotov et al., Figure 2

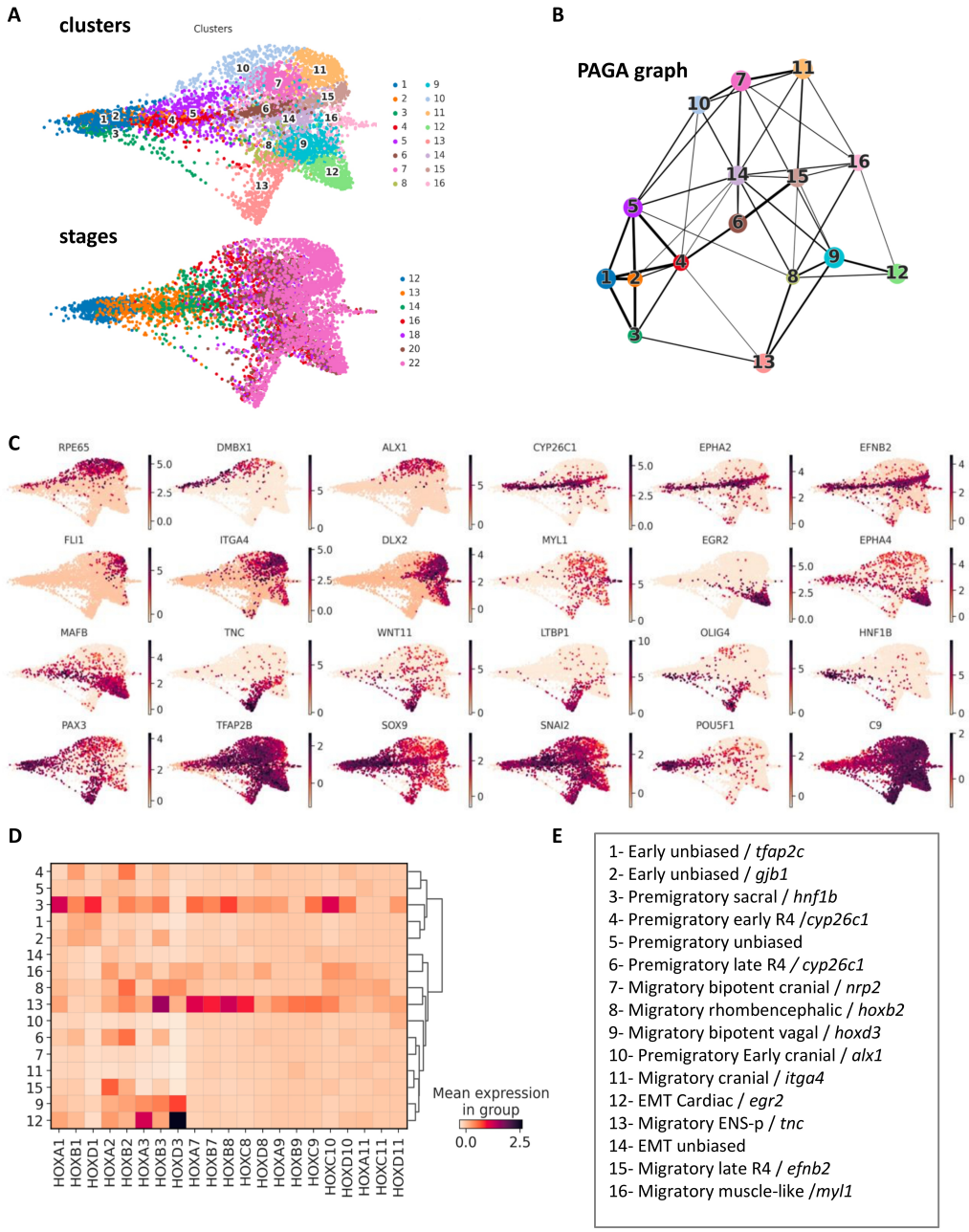

Fig. 2. Premigratory neural crest transcriptome heterogeneity. (A) Forced-directed graph for the NC dataset (Leiden clustering) revealed 16 distinct states (clusters) before and during EMT (developmental stages 12-22). **(B)** Principle Graph analysis (PAGA) estimates clusters connectivity which is strong during NC induction stages 12-13, yet showing early NC heterogeneity, with early emergence of *cyp26c1*$^{+}$ clusters #4/6/15 and ENSp cluster #3. Line thickness increases with higher connections **(C)** Expression of key cluster-specific genes, including *rpe65, dmbx1, alx1* (#10), *cyp26c1, epha2, efnb2* (#4/6/15), *fli1, itga4, dlx2* (#11), *egr2, epha4, mafb* (#12), *tnc, wnt11, ltbp1* (#13), early *olig4, hnf1b* (#3*)* and muscle-like NC specific *myl1* (#16). Genes expressed broadly in NC cells define a "canonical NC" signature: early *pax3, tfap2b, sox9, snai2, and c9*. Multipotency-related genes are present mostly until mid-neurula stage *(pou5f1)*. **(D)** The hox gene signature of each cluster provides its approximate position along the antero-posterior body axis. **(E)** Each cluster's main expression characteristics used to name them.

1234

Kotov et al., Figure 3

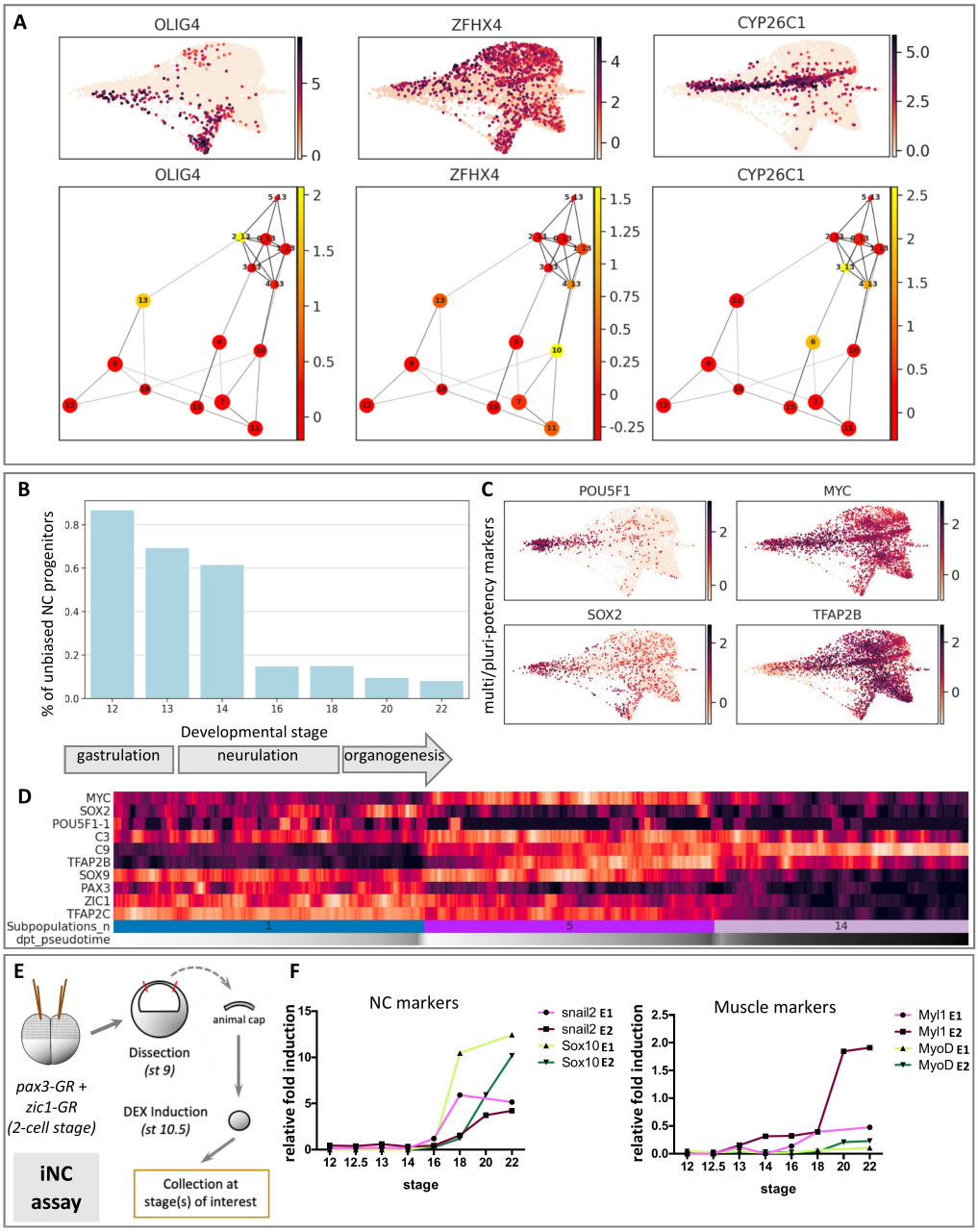

Fig. 3. Emergence of heterogeneity from unbiased NC during NC induction. (A) From the end of gastrulation, three previously undescribed early trends emerge. Clustering of stage 13 cells only, followed by PAGA analysis identified their similarities with the stage 20-22 clusters: an *olig4*-enriched subpopulation linked to ENSp cluster #13; a *zfhx4*-enriched cluster related to *rpe65*$^{+}$ cluster #11 and a third stage 13 subpopulation expressing *cyp26c1* linked to the cranial NC branch #4, #6, #15. **(B, C, D)** Until mid-neurulation (st. 14), most cranial and vagal NC cells expressed a canonical NC stem cell-like signature (*sox9, tfap2c, snai2)* together with high expression of pluripotency markers (*e.g. pou5f1, cmyc,* and *sox2).* No indication of bias toward a specific fate was detected in clusters #1, #5 and EMT-stage cluster #14. (B) Expression patterns in pseudotime for unbiased clusters #1, #5, #14; B) Proportions of the unbiased cells in the NC dataset; C) UMAP plots. **(E, F)** At early migration stage (20-22), cluster 16 expresses myosin-like genes. Direct NC induction in ectoderm explants *in vitro* (iNC assay) followed by RTqPCR, identifies *myoD* and *myl1* expression at a similar stage.

1251

Kotov et al., Figure 4

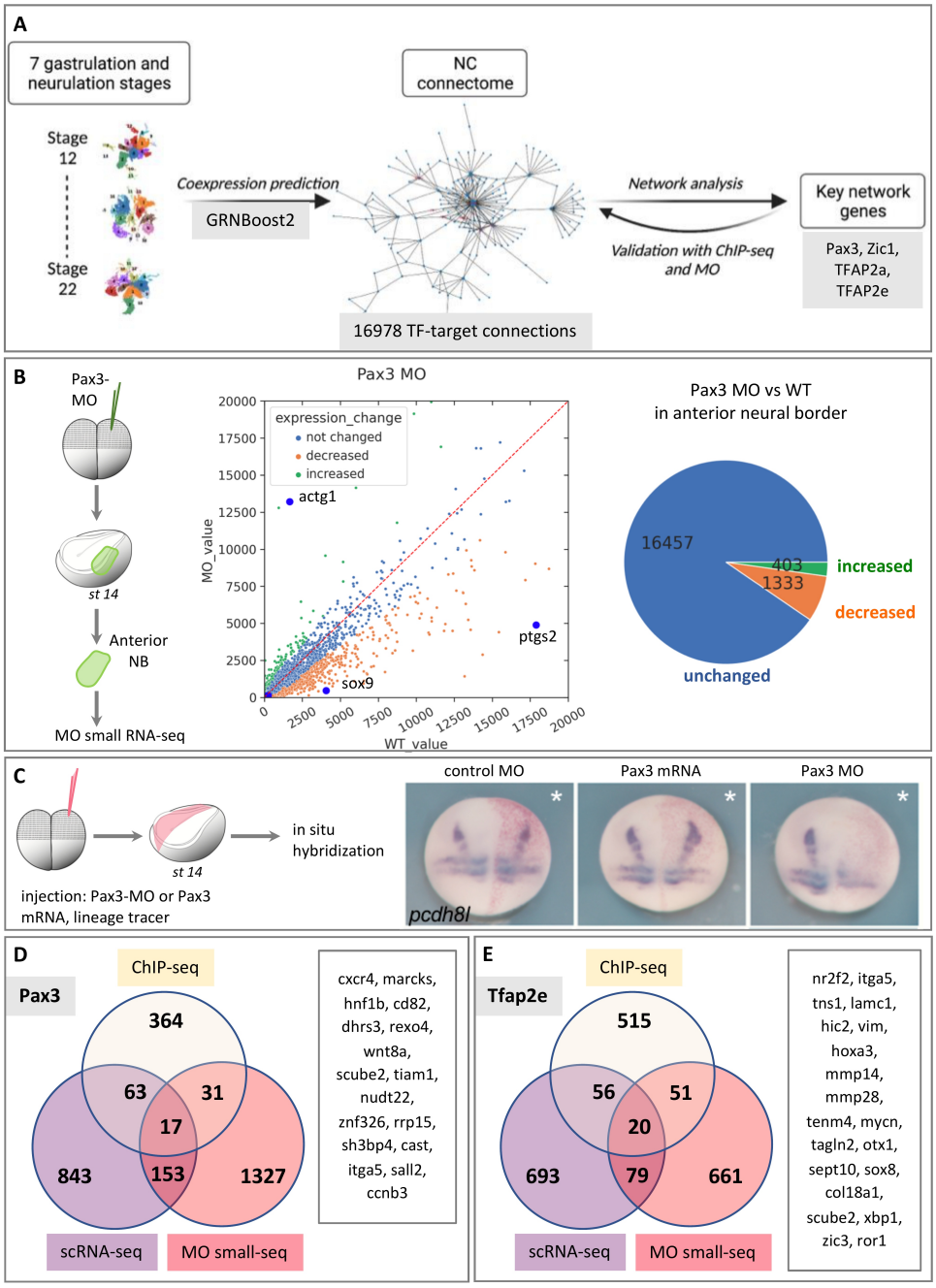

Fig. 4. NC connectome generation and validation. (A) NC cells from all stages were used to build a large-scale connectome with GRNBoost2. ChIP-seq and MO knockdown small RNA-seq were used to validate a significant number of links predicted for *pax3, tfap2e, tfap2a and zic1*. **(B)** Overview of *pax3* MO analysis in NB/NC. Most affected genes were decreased indicating that Pax3 mostly displays transcriptional activation action in NC. **(C)** *Pcdh8l,* a target of Pax3 is regulated by Pax3 gain-of-function (mRNA) and loss-of-function (MO) *in vivo*. ISH, Injected side is traced in red. **(D, E)** Venn diagrams of target genes validated by ChIP-seq and MO-small-seq for *pax3* (D) and *tfap2e* (E). Genes linked to *pax3* and *tfap2e* by the three methods are listed.

1262

Kotov et al., Figure 5

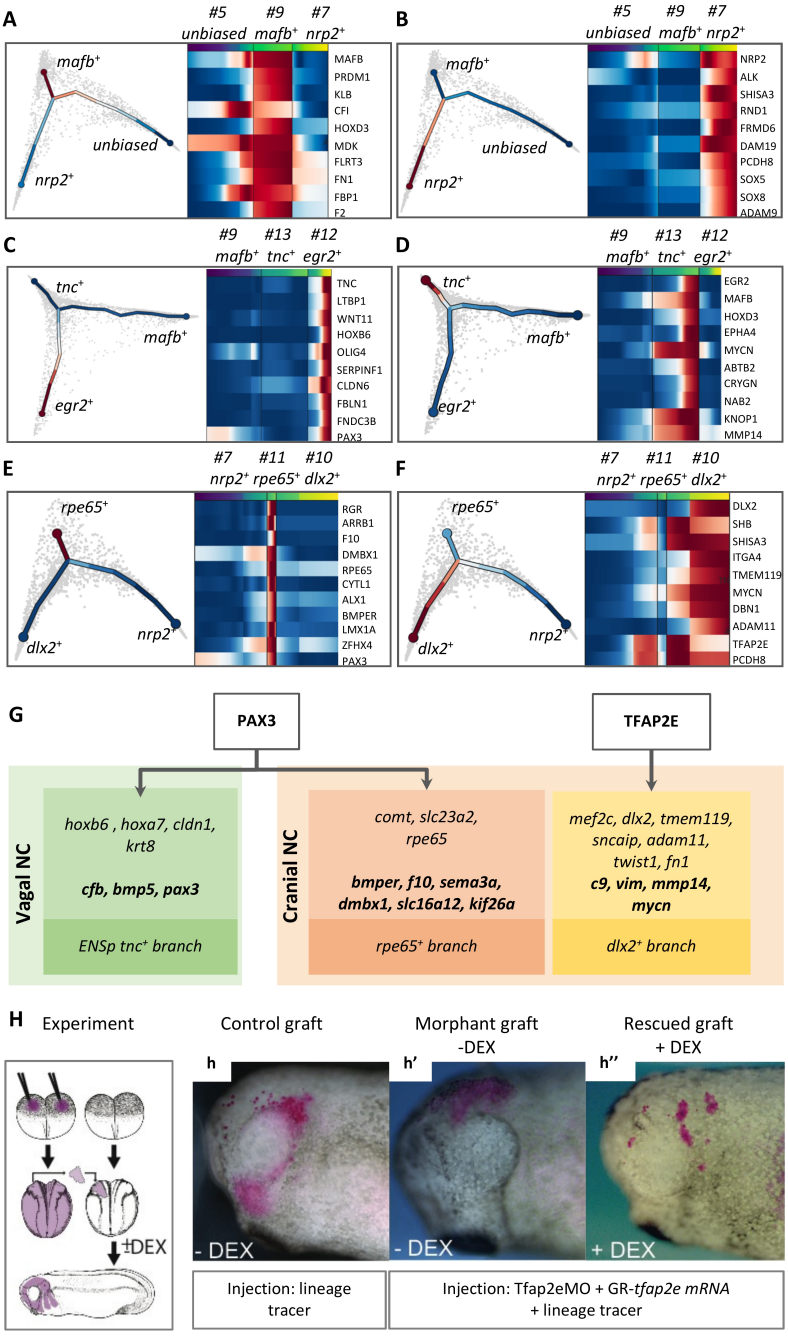

Fig. 5. NC branching analysis. Cells sub-selected around a chosen bifurcation point were analyzed using tree inference, advanced pseudotime downstream analysis, and scFates. Gene programs for bifurcation of premigratory unbiased cluster #5 into clusters #7 **(A)** and #9 **(B);** of migratory bipotent vagal cluster #9 into clusters #12 **(C)** and #13 **(D)** and of migratory bipotent cranial cluster #7 into clusters #11 **(E)** and #10 **(F). (G)** MO-mediated depletion and ChIP-seq validate Pax3 function in both vagal (clusters #12 vs #13) and cranial (#11 vs #10) branching, and TFAP2e function in cranial (#10 vs #11) branching. **(H)** Premigratory NC (pink) was grafted into host embryos. In comparison to control (h), TFAP2e morphant NC (h') does not emigrate towards craniofacial areas. Activation of TFAP2e-GR in morphant cells upon EMT stage restores migration (h'').

1275

Kotov et al., Figure 6

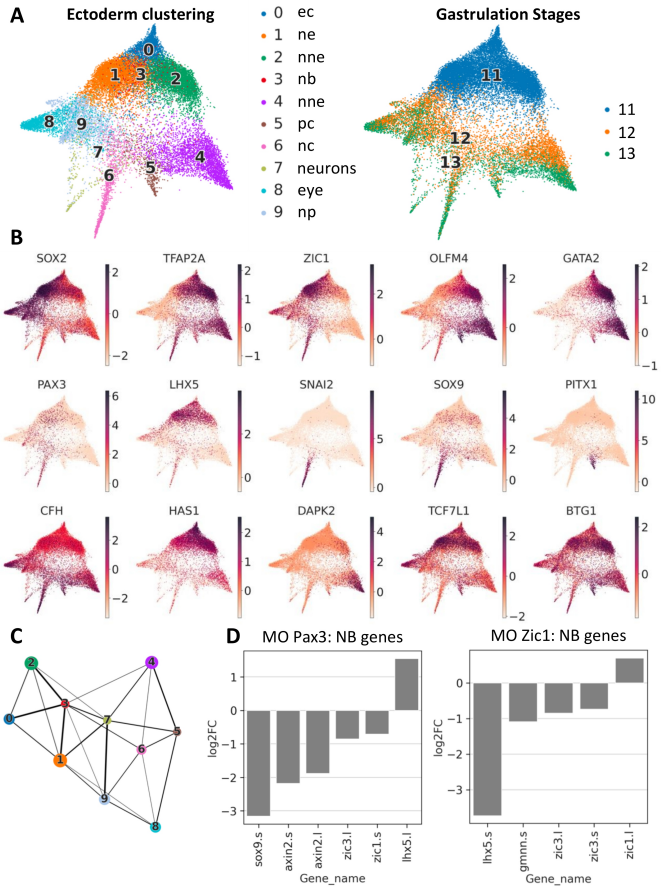

Fig. 6. Ectoderm dataset analysis. (A) Leiden clustering using 17138 early ectoderm cells from 11, 12, 13 NF stages. *0) Ectoderm stage 11; 1) neural ectoderm; 2) non-neural ectoderm; 3) NB zone; 4) non-neural ectoderm stage 13; 5) placodes; 6) neural crest; 7) neurons; 8) eye primordium; 9) neural plate.* **(B)** UMAP plots of key genes in the Ectoderm dataset. **(C)** PAGA plot for Ectoderm dataset reveals a central role of the NB zone (3) between ne, nne, nc and pc. **(D)** The NB signature is affected by Pax3 or Zic1 depletion.

1283

Kotov et al., Figure 7

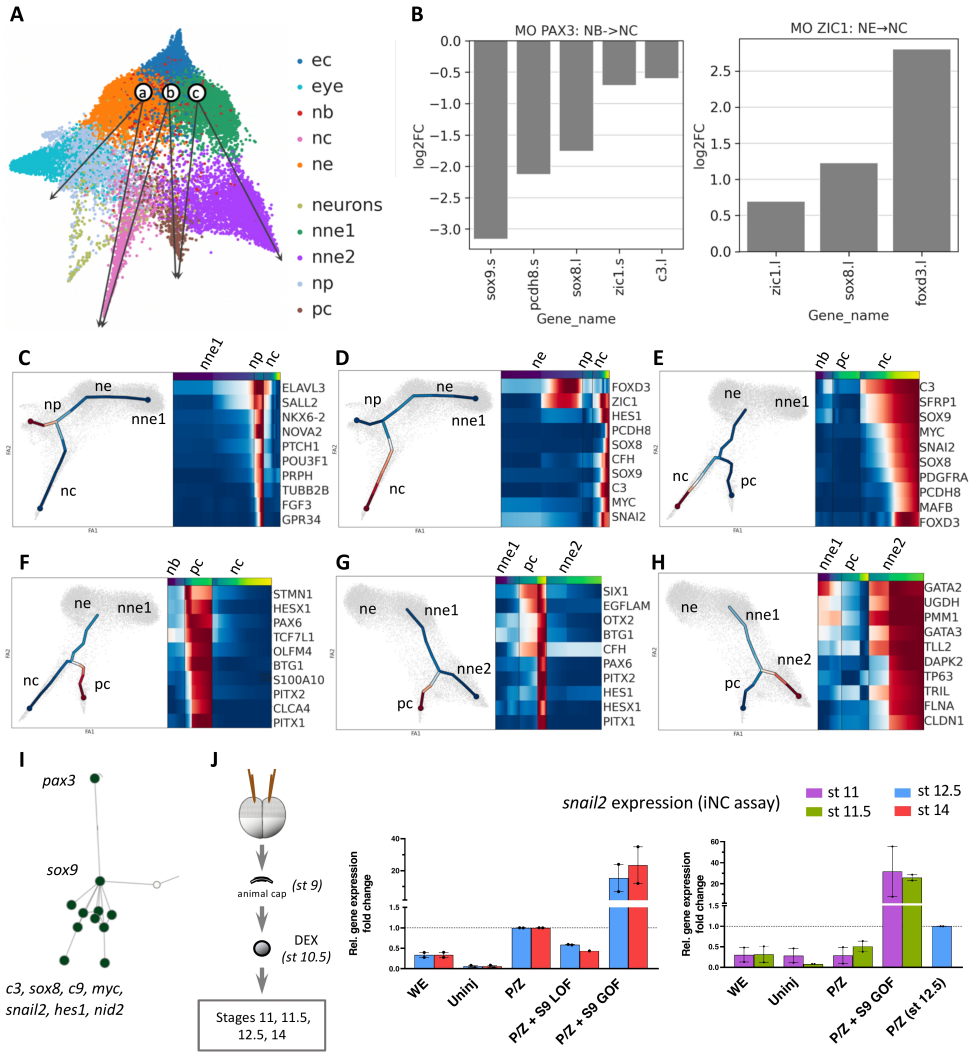

Fig. 7. Ectoderm branching and validation of Sox9 early role in NC induction. (A) Branching analysis retrieves the possible gene programs for NC and PC development at stages 11-13, considering two sources of origin for both populations: NP and NB for NC, and NNE and NB for PC. It revealed that Zic1 is an important (connectome) and early gene for branch NE->NC, while Pax3 is early gene for branch NB->NC. Pax3 depletion impacts expression of several branch-specific genes, including *sox9, foxd3,* as well as *zic1* while Zic1 depletion increases *sox8* and *foxd3*. **(C)** NNE1->NP gene program, **(D)** NE->NC gene program, **(E)** NB->NC gene program, **(F)** NB->PC gene program, (**G)** NNE1->PC gene program, **(H) NNE1->**NNE2 gene program..**(I)** NB connectome analysis suggested a novel epistasis relationship between *pax3*, *sox9* and other downstream NC specifiers. **(J)** In iNC assay, Sox9 acts downstream of Pax3 and is essential for activating the downstream NC program. Additionally, at gastrula stages, a time point at which *pax3*/*zic1* activation does not yet induce *snail2* expression in iNC, adding Sox9 activation is sufficient to obtain high levels of *snail2* precociously. RT-qPCR analysis showing relative *snail2* expression fold change in iNC at late gastrula and early neurula stages. WE - whole embryo; Uninj - uninjected animal caps; P/Z - *pax3*-GR + *zic1*-GR iNC; S9 LOF - *sox9* loss-of-function (LOF) or gain-of-function (GOF).

1304

Kotov et al., Figure 8

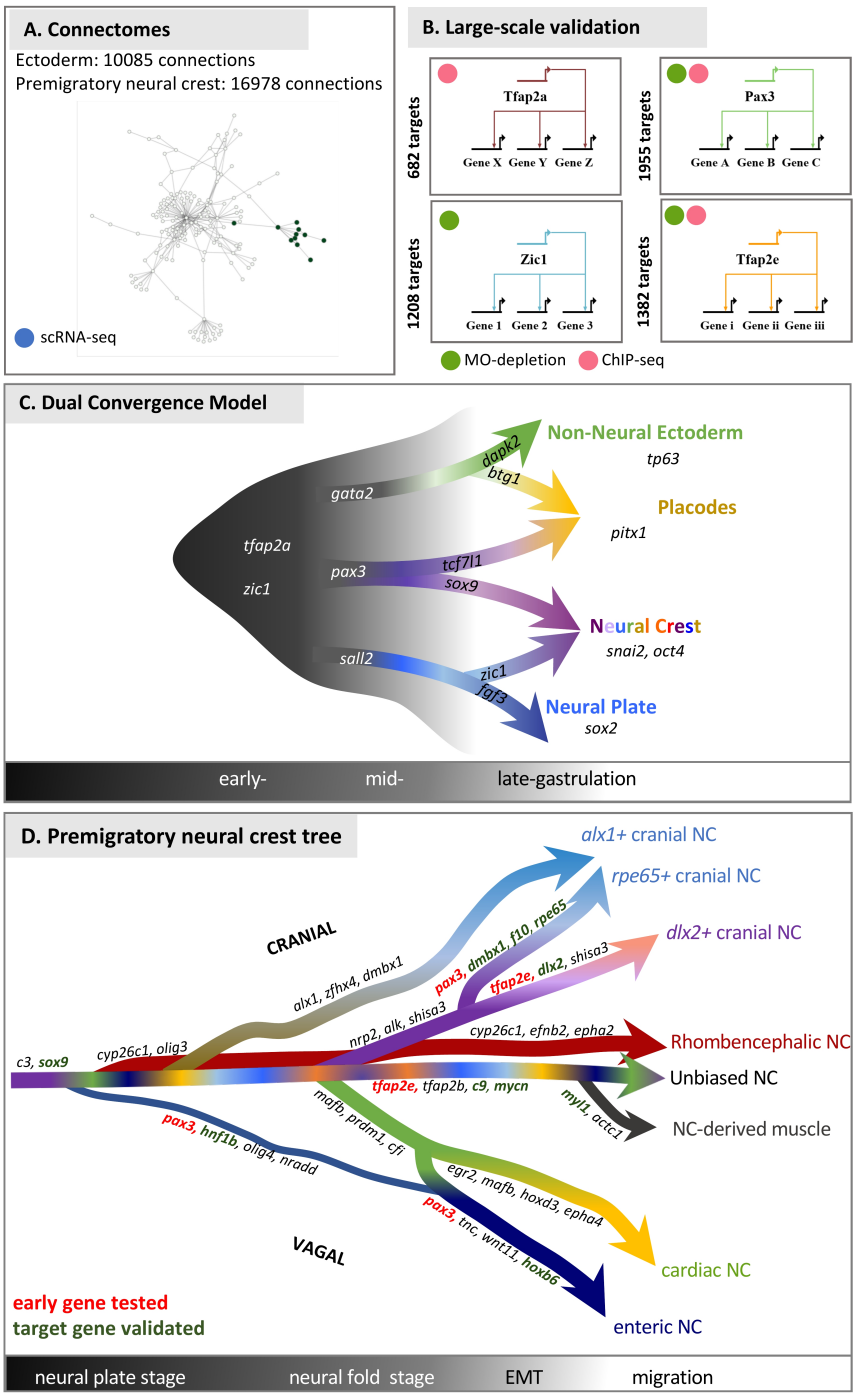

Fig. 8. Neural crest GRN and developmental trajectories. (A) GRNBoost2-predicted connectomes for Ectoderm (gastrula stage) and Neural crest (neurulation stage). **(B)** RNA-seq on dissected neural border/neural crest explants or ChIP-seq provide large-scale GRNs linked to Pax3, Zic1, TFAP2a, and TFAP2e. **(C)** At gastrula stage (time line indicated), the neural border cells expressing *tfap2a, zic1*and *pax3* present trajectories towards placodes and neural crest. Those trajectories converge with a trajectory from neural plate towards neural crest and another one from non-neural ectoderm towards placodes. Branching analysis highlights a gene signature underlying those transcriptome transitions (the top gene is indicated here). (D) Lineage tree of the neural crest cells, from the end of gastrulation, during neurulation and upon epithelial-mesenchymal transition, ending at early migratory stage (time line indicated). Gene signatures supporting each trajectory is summarized. The function of transcription factors expressed prior branching (Pax3, Tfap2e, red) was validated on expression of genes expressed after branching (green).

Table 1. Highly connected genes in the GRNboost2 neural crest network.

Gene	Degree centrality	Betweeness centrality	Max. expression stage	NC specificity
TFAP2C	28.028933	21.510673	12	6.59
ZIC3	16.455696	7.885226	12	3.73
ZIC1	8.137432	2.351524	12	9.34
ZIC2	7.233273	2.026896	12	3.62
DMBX1	3.616637	11.876445	12	1.57
PAX3	3.435805	2.211830	12	5.93
SOX9	11.573237	8.575830	13	14.07
OLIG4	4.882459	2.642370	13	4.54
MAFB	7.956600	4.174946	14	09.08
SNAI2	5.244123	0.927599	14	20.03
SOX8	4.520796	2.071516	14	20.60
RPE65	1.446655	0.534404	14	6.49
TFAP2B	8.499096	4.135991	16	25.47
HOXB3	3.978300	0.959282	16	2.35
SOX10	3.797468	0.705758	16	15.40
NR6A1	3.797468	0.706433	16	9.18
ZFHX4	2.169982	0.791908	16	4.83
ALX1	2.169982	1.627017	16	3.69
EPHA2	1.989150	1.403078	18	3.77
E2F3	1.446655	2.256467	18	0.68
TFAP2E	5.786618	1.850976	20	15.21
EGR2	5.424955	2.505897	20	5.96
MYCN	17.359855	12.737248	22	8.81
DLX2	12.839060	8.413243	22	6.88
HOXD3	8.137432	3.417475	22	4.96
EEF1D	4.701627	0.795235	22	9.55
ZBTB16	3.074141	1.013930	22	2.80
TFEC	2.169982	0.562422	22	0.10
VIM	2.169982	0.879581	22	2.43

1323
1324

Table 2. Highly connected genes in the GRNboost2 ectoderm network

Gene	Degree centrality	Betweeness centrality	Mean nc/pc/nb specificity	NC specificity	PC specificity	NB specificity
TFAP2C	70.319635	6.203872	8.778883	17.587187	3.636364	5.113099
TFAP2A	67.123288	5.770185	11.238043	4.836522	-0.884711	29.762320
ZIC1	47.488584	1.674848	15.645578	18.120411	-8.226690	37.043015
HES1	30.136986	0.815641	13.273738	27.994427	11.076355	0.750431
SOX9	24.657534	0.463349	11.848502	38.367329	-4.275626	1.453803
MYC	17.808219	0.340629	9.269785	22.733620	4.699314	0.376421
SNAI2	17.579909	0.192783	7.027262	27.004408	-3.017278	-2.905344
PITX1	16.438356	0.115279	5.463268	-3.656815	21.928877	-1.882259
PAX3	14.611872	0.172905	5.509155	15.614752	-3.379381	4.292094
SOX8	12.100457	0.094409	5.176289	19.021635	-2.535636	-0.957131
C3	9.817352	0.019518	12.694010	36.559040	6.013386	-4.490397

From neural border to migratory stage: A comprehensive single cell roadmap of the timing and regulatory logic driving cranial and vagal neural crest emergence

Supplementary Materials

Aleksandr Kotov, Mansour Alkobtawi†, Subham Seal†, Vincent Kappès, Sofia Medina, Hugo Arbès, Richard Harland, Leonid Peshkin, and Anne H. Monsoro-Burq*

*Corresponding author. Email: anne-helene.monsoro-burq@curie.fr

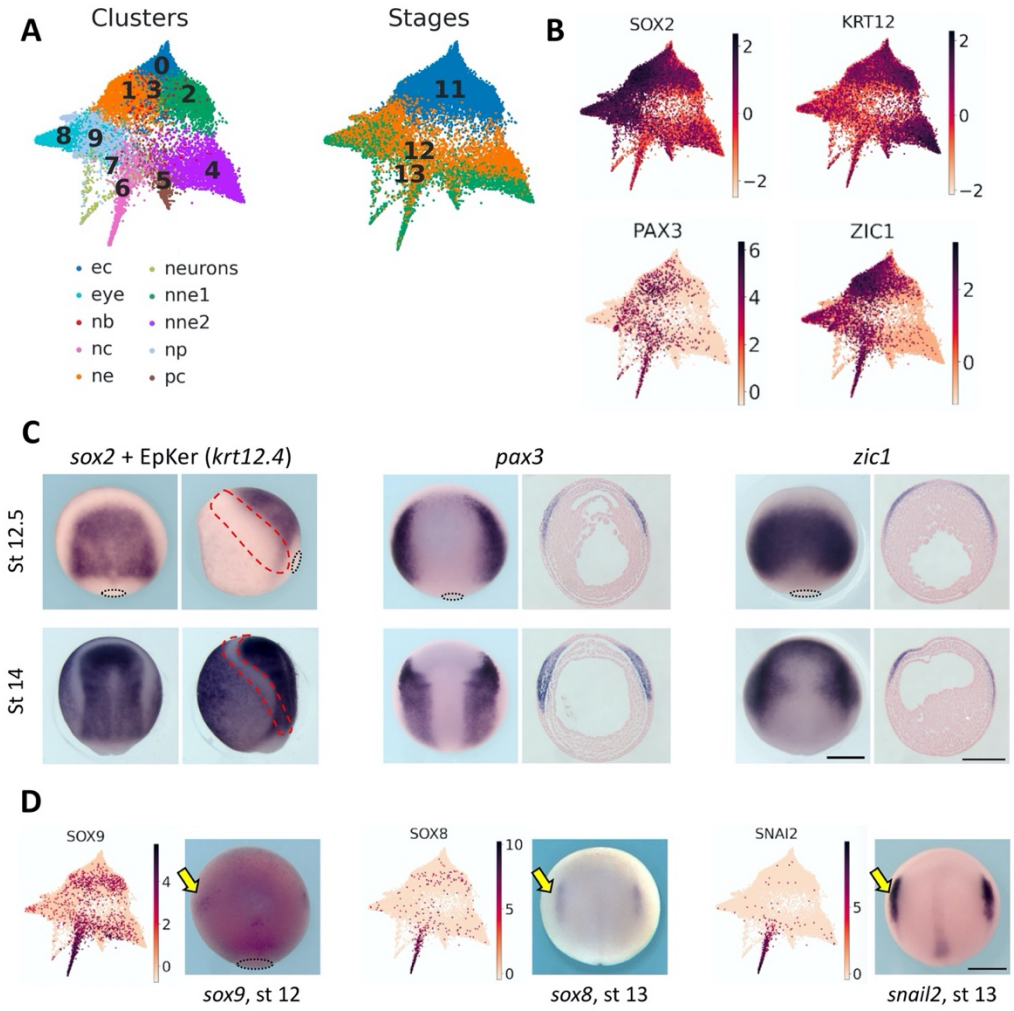

Fig. S1. **Markers for NB zone and early NC.**
(A) Ectoderm UMAP plots for stages 11,12 and 13 depicting different clusters and their corresponding stage. (B) Gene markers for the 3 major ectoderm derivatives. *sox2* marks the neural ectoderm while *krt12* (epidermal keratin 12) marks the non-neural ectoderm. Unlike the other derivatives, the NB zone does not yet have a strictly specific gene marker and is usually depicted by *pax3* expression or the overlapping expressions of genes like *tfap2a* and *zic1*. (C) ISH images of embryos at stage 12.5 (late gastrula) and stage 14 (mid neurula) depicting the gene markers for the ectoderm derivatives mentioned in (B). The red dotted region depicts the neural border zone, devoid of both *sox2* and *krt12* expression. Scale bar, 500 μm. (D) EC UMAP and corresponding ISH images depict the earliest stages of detection of 3 well-known early NC markers. *Sox9* is initiated at the prospective NC zone at stage 12. *Sox8* and *snail2* are detected at the early NC at stage 13. Yellow arrows point to the NC region. Scale bar, 500 μm.

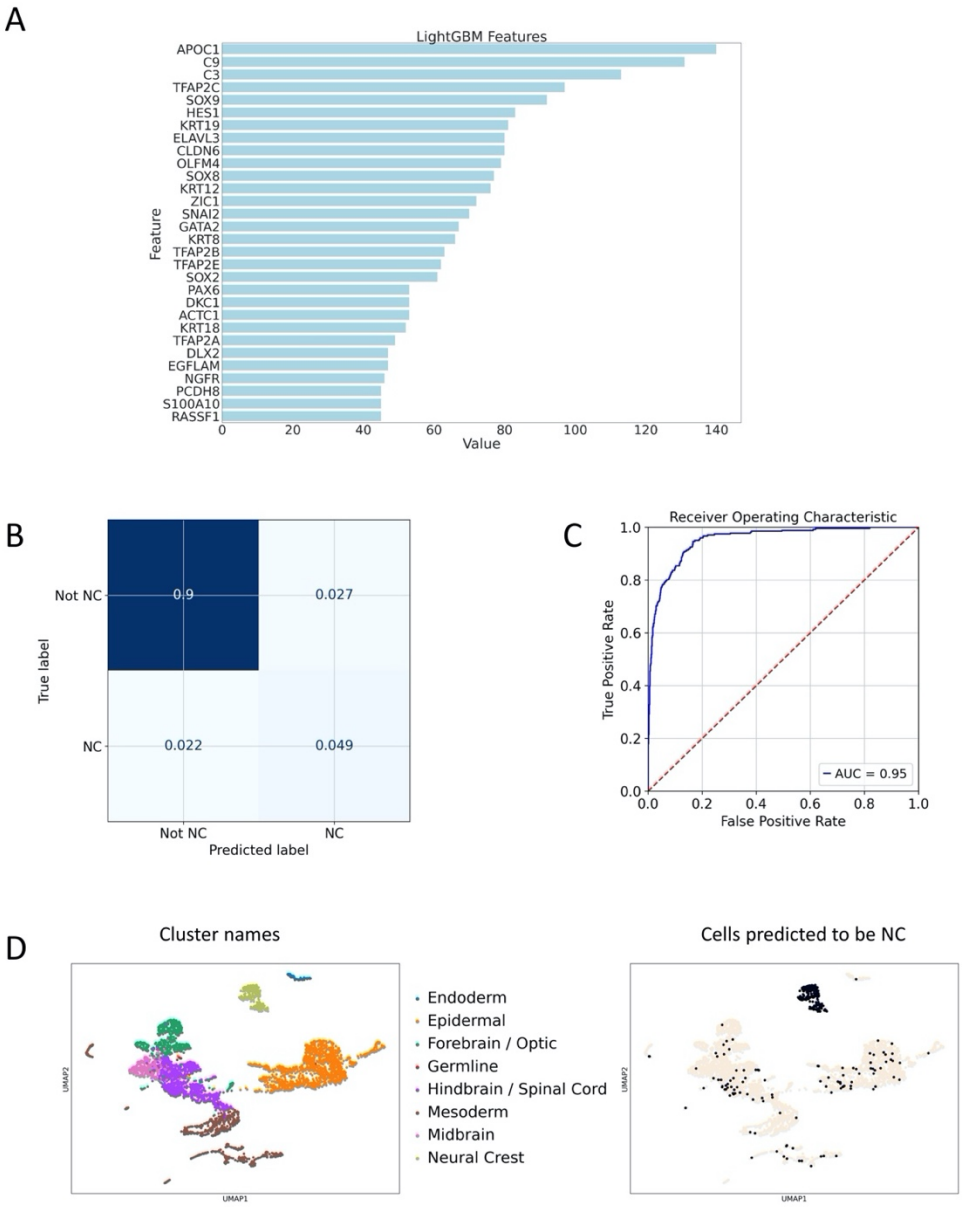

Fig. S2. **LightGBM NC classifier.**
LightGBM-based binary classificator for the NC cells. Using the whole embryo data matrix of gene expression, we have selected the top 10% LightGBM model important features for NC detection. In order to validate it in the Zebrafish dataset (21), we only kept genes that were in the Zebrafish dataset. Using only top features, we re-built the model (test results: 0.99 accuracy and 0.90 f1 score) and validated it in Zebrafish dataset with the accuracy 0.95 and f1 score 0.66 in 14 stage cells. **(A)** Top features for NC classification using LightGBM model. **(B)** Confusion matrix for validation in Zebrafish dataset for stage 14. **(C)** ROC curve for binary NC classifier predicted scores. **(D)** UMAP for Zebrafish 14 stage cells with model predicted cells as NC. Prediction accuracy is enough for detection of cluster of interest (NC) despite of technical and biological batch effect between Xenopus and Zebrafish datasets.

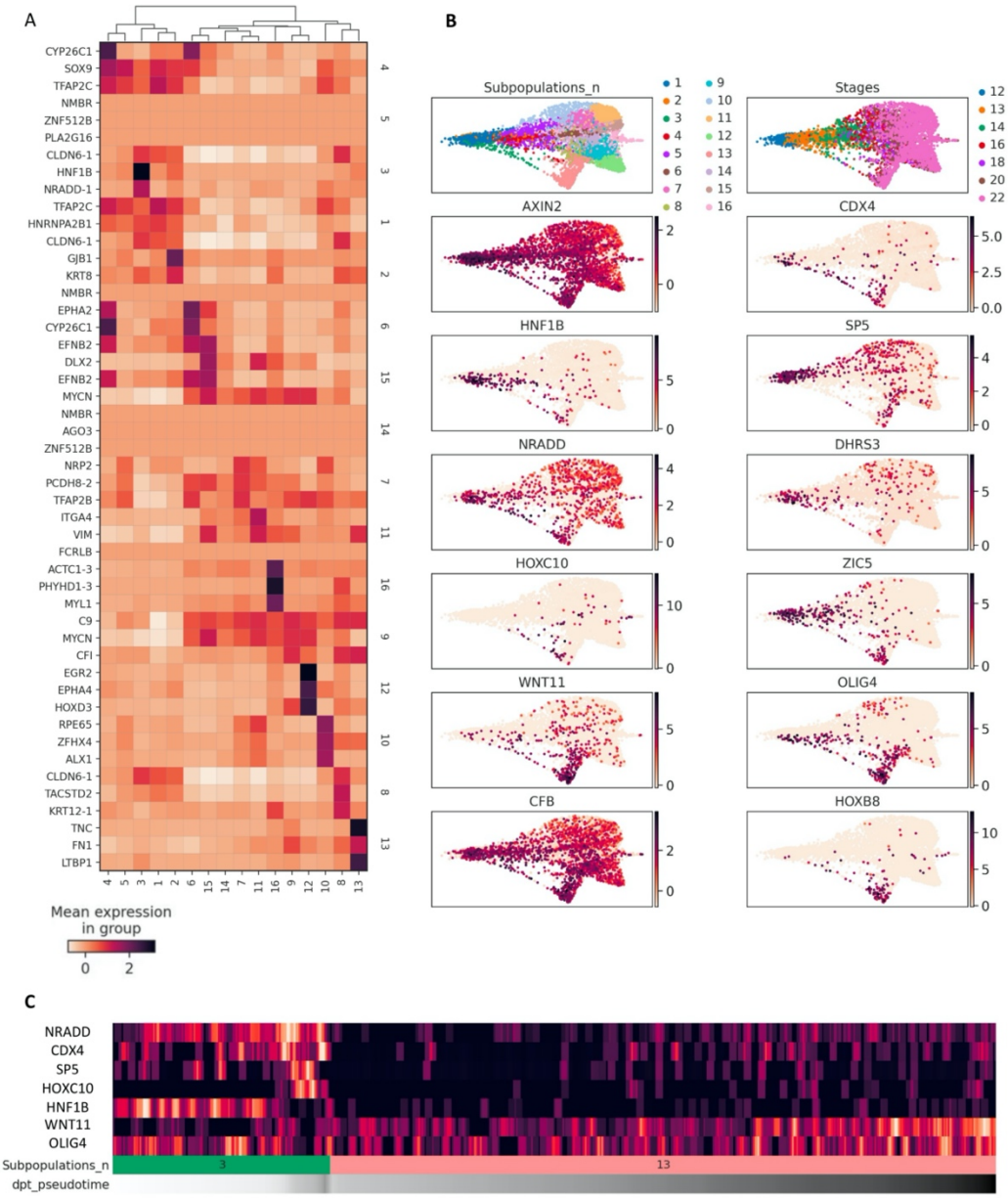

Fig. S3. **Cluster-specific genes.**
(A) Matrixplot with the top 3 specific genes per cluster for the Neural Crest dataset. **(B)** UMAP plots for the early-biased NC subpopulation expressing *hnf1b*, *cdx4*, *nradd* and posterior hox genes. In addition to cluster-specific *hnf1b* and *olig4*, *dhrs3* is co-expressed with *zic5* which specifically stays active during the whole "sacral" trajectory from stage 12 to late ENSp. Generally, *dhrs3* is expressed in cells that do not express *cyp26c1*. *Dhrs3* thus participates since stage 12 to a strong demarcation, earlier than posterior HOX expression appearing later. **(C)** Expression of cluster 3 specific genes along the pseudotime.

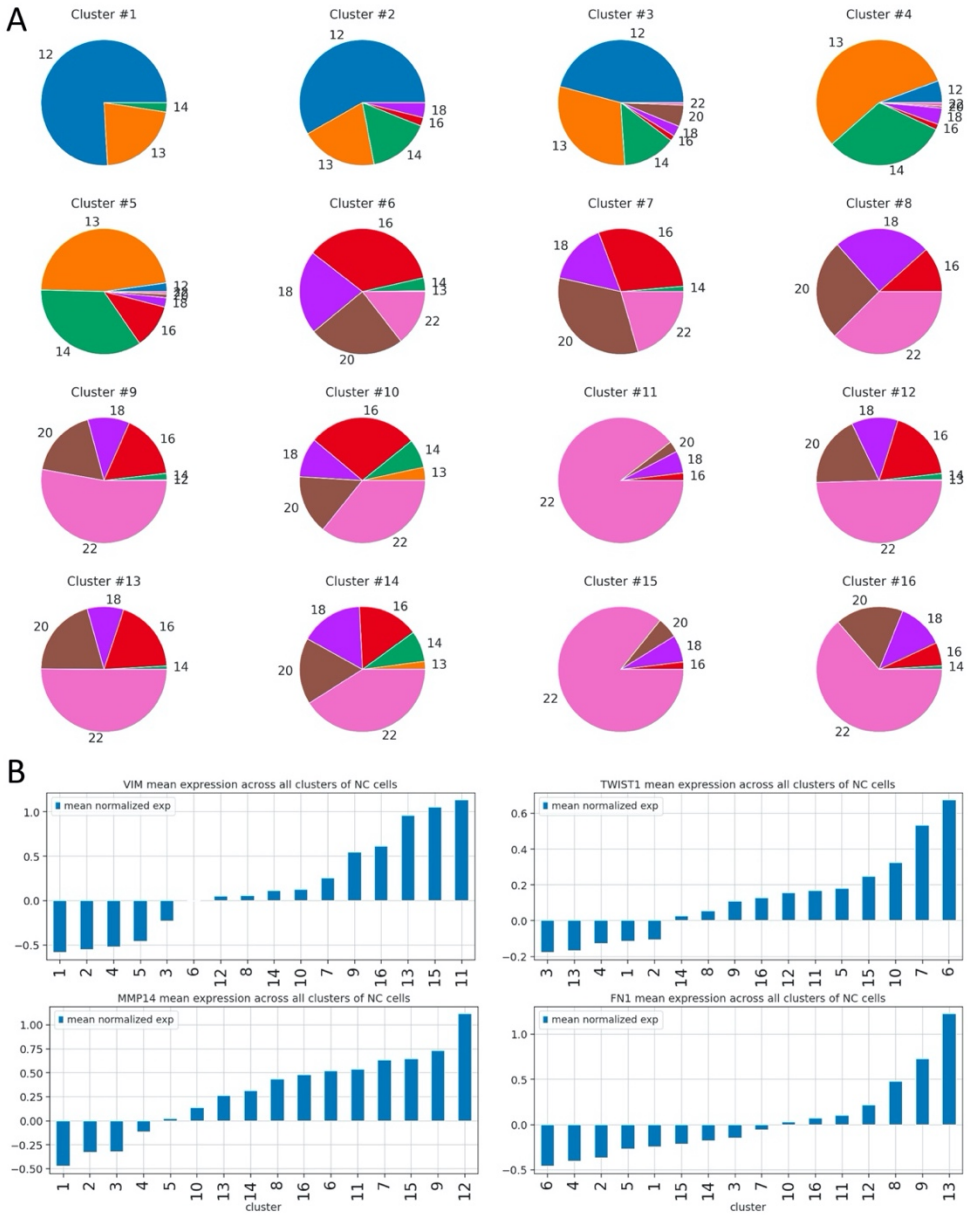

Fig. S4. **Developmental stages and expression of EMT markers per cluster.**
(A) Pieplots represent the proportion of cells at each stage in each cluster. Some clusters include cells of 6 stages, e.g. cluster 10. **(B)** Each cluster presents various levels of expression of EMT and migration regulators. Bar plots with mean normalized expression for each cluster for *vim, twist1, mmp14* and *fn1*.

Kotov et al, Supplementary Figure S5

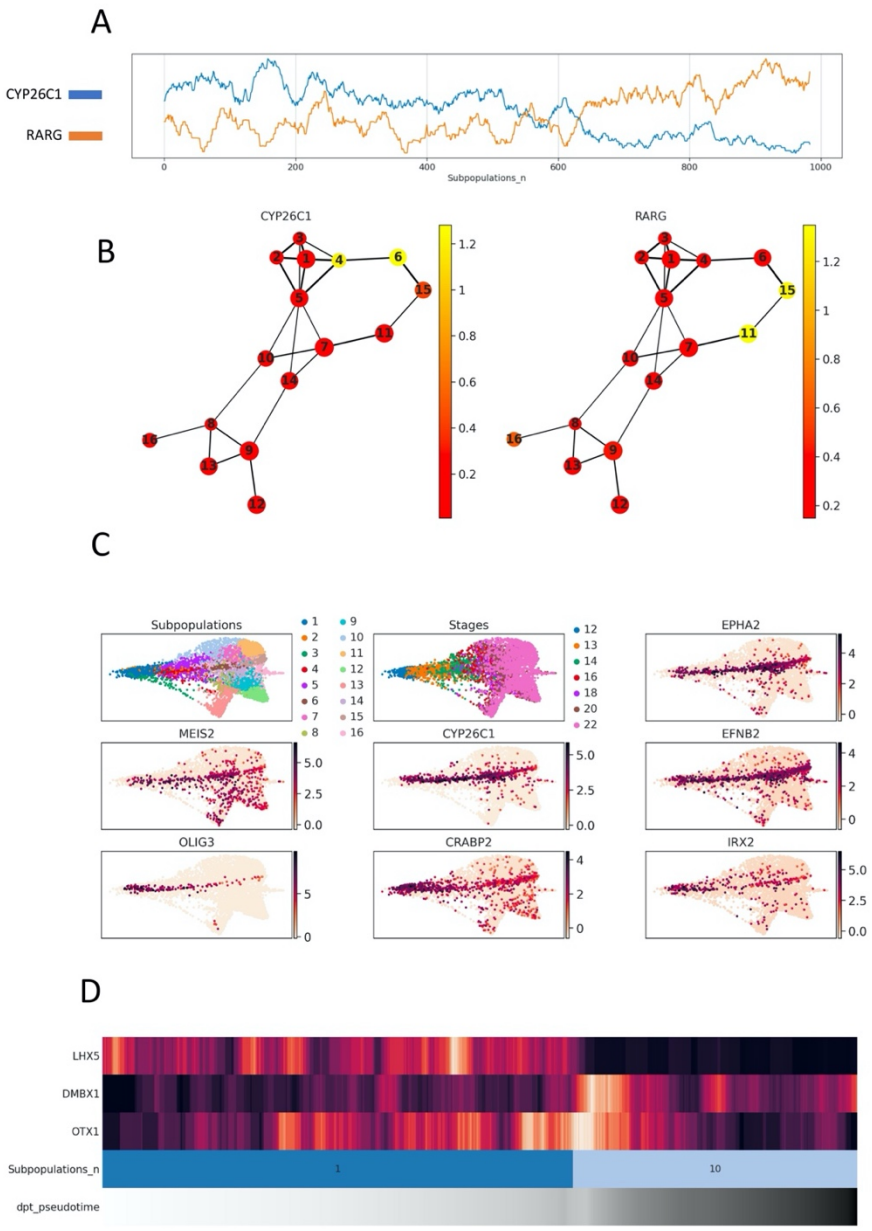

Fig. S5. **Early posterior enteric cluster #4 and related late clusters #6, #15.**
(A) Line Plot for expression dynamics for cluster 4, 6, 15, representing the relationships between *rarg* and *cyp26c1*. Cells within clusters are sorted according to pseudotime. **(B)** PAGA plot with *rarg* and *cyp26c1* mean expression. **(C)** Key specific genes for RA stream (clusters 4, 6 and 15). In the middle RA-dependent cluster #6, we observed increased expression of *crabp2*, which delivers all-trans retinoic acid to retinoic acid receptors (RARs, RXRs). Interestingly, during NC induction *crabp2* is expressed homogeneously in unbiased NC and early RA-dependent CNC, but later the *crabp2* expression remains only in the *cyp26c1*$^{+}$ stream. **(D)** Expression heatmap for early cranial cluster 10 markers *dmbx1* and *otx1* and multipotent cluster 1 marker *lhx5*.

Kotov et al., Supplementary Figure S6

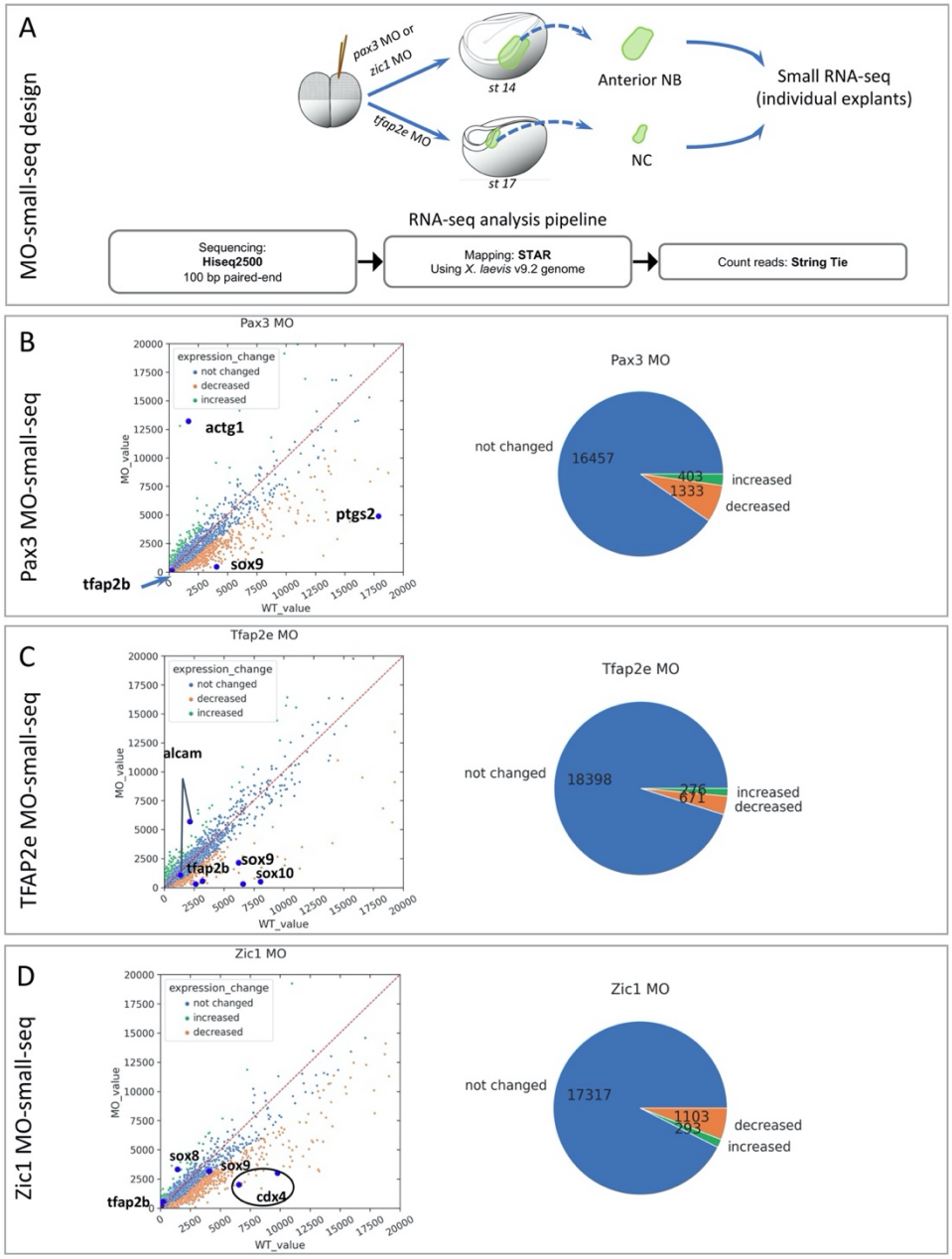

Fig. S6. **MO experiments overview.**
We performed MO knockdown experiments for the main genes from the predicted networks for NC dataset. We revealed 1333 decreased genes in comparison to 403 increased genes in *pax3* MO which confirms the mostly activating role of Pax3. For Zic1 and TFAP2e, similar proportions of increased/decreased genes are observed. **(A)** Design of MO-small-seq experiments. **(B, C, D)** General statistics for changed and unchanged genes after Pax3, Tfap2e, or Zic1 depletion compared to controls.

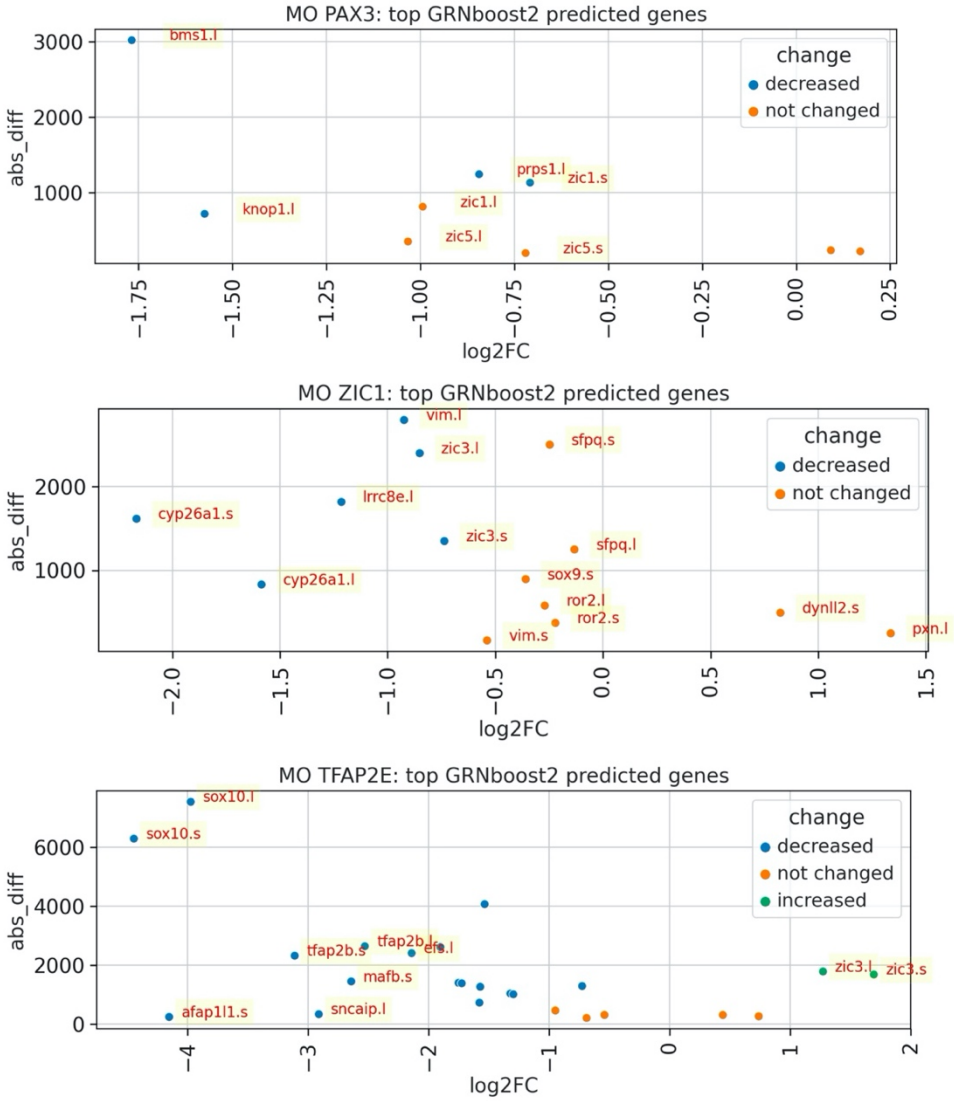

Fig. S7. **Top GRNboost2-predicted linked genes for Pax3, Tfap2e and Zic1 which also changed in MO samples.** We intersected results of the scRNA-seq predictions and MO knockdown experiments. Plots represent the top genes from the intersection for the several main actors (Pax3, Tfap2e, Zic1) from the predicted network. Among them *bms1* for Pax3, *sox10* for Tfap2e and *cyp26a1* for Zic1.

Kotov et al., Supplementary Figure S8

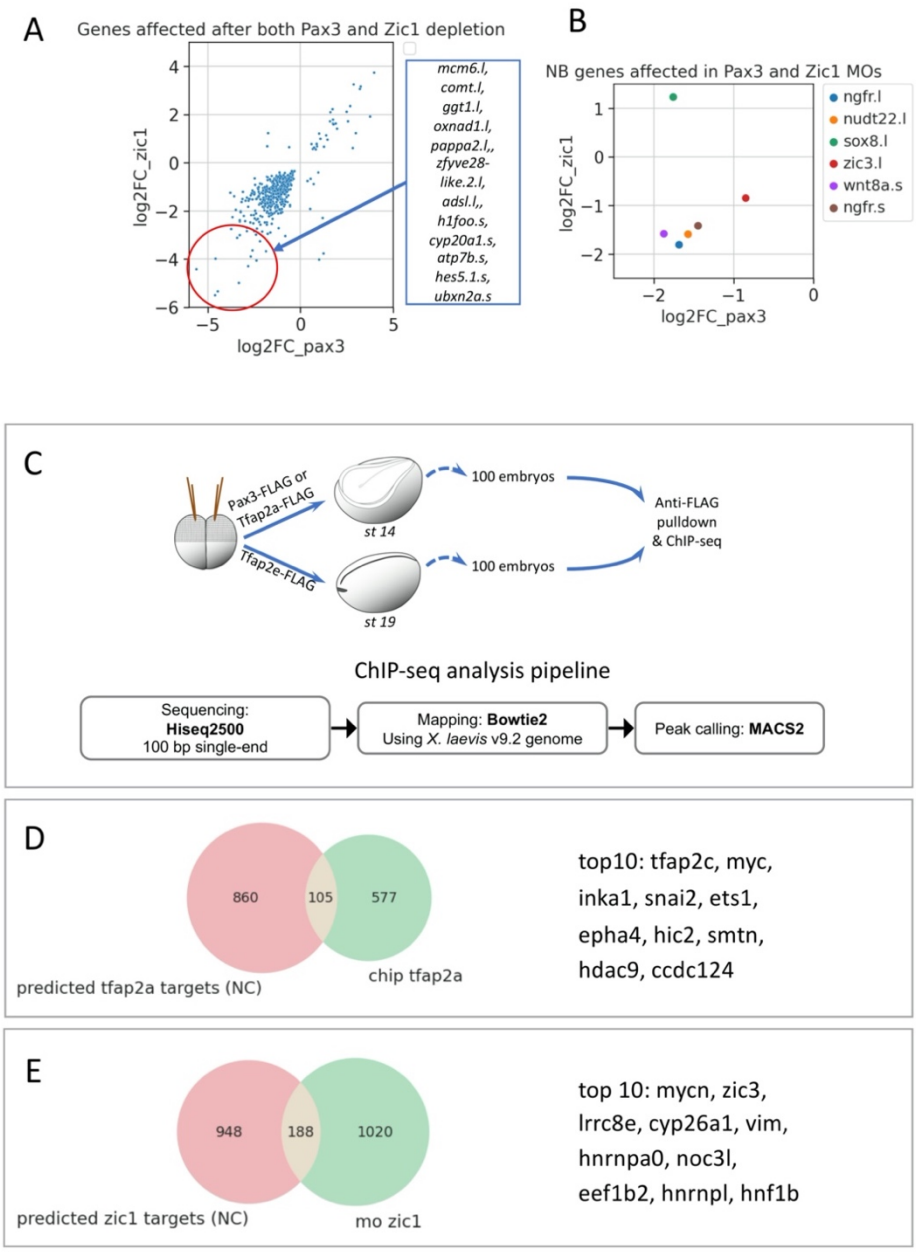

Fig. S8. **Direct gene regulation by Tfap2a, Zic1 and Pax3 during the NC induction.** In order to reveal direct targets and validate scRNA-seq prediction, we performed ChIP-seq for Tfap2a (one of the main actors in the Ectoderm network), Pax3 and Tfap2e (main actors in the NC network). ChIP-seq was performed in whole embryos (WE) then genes which are expressed in the NC cells were selected. **(A)** General overview of the most changed genes in both Pax3 and Zic1 MO samples (abs_diff>300), most of them decreased. **(B)** Genes from the NB zone signature with the lower expression level threshold. It shows that both Zic1 and Pax3 are needed for activation of *ngfr, wnt8a, sox8* and *nudt22* expression. **(C)** ChIP-seq analysis pipeline. **(D, E)** Comparison between GRNBoost2-based predictions and experimental validation for Tfap2a (ChIP-seq) and Zic1 (MO knockdown). Around 12% of genes predicted to be linked to Tfap2a are found as direct targets; while about 20% of predicted Zic1 linked genes are affected by Zic1 depletion *in vivo*.

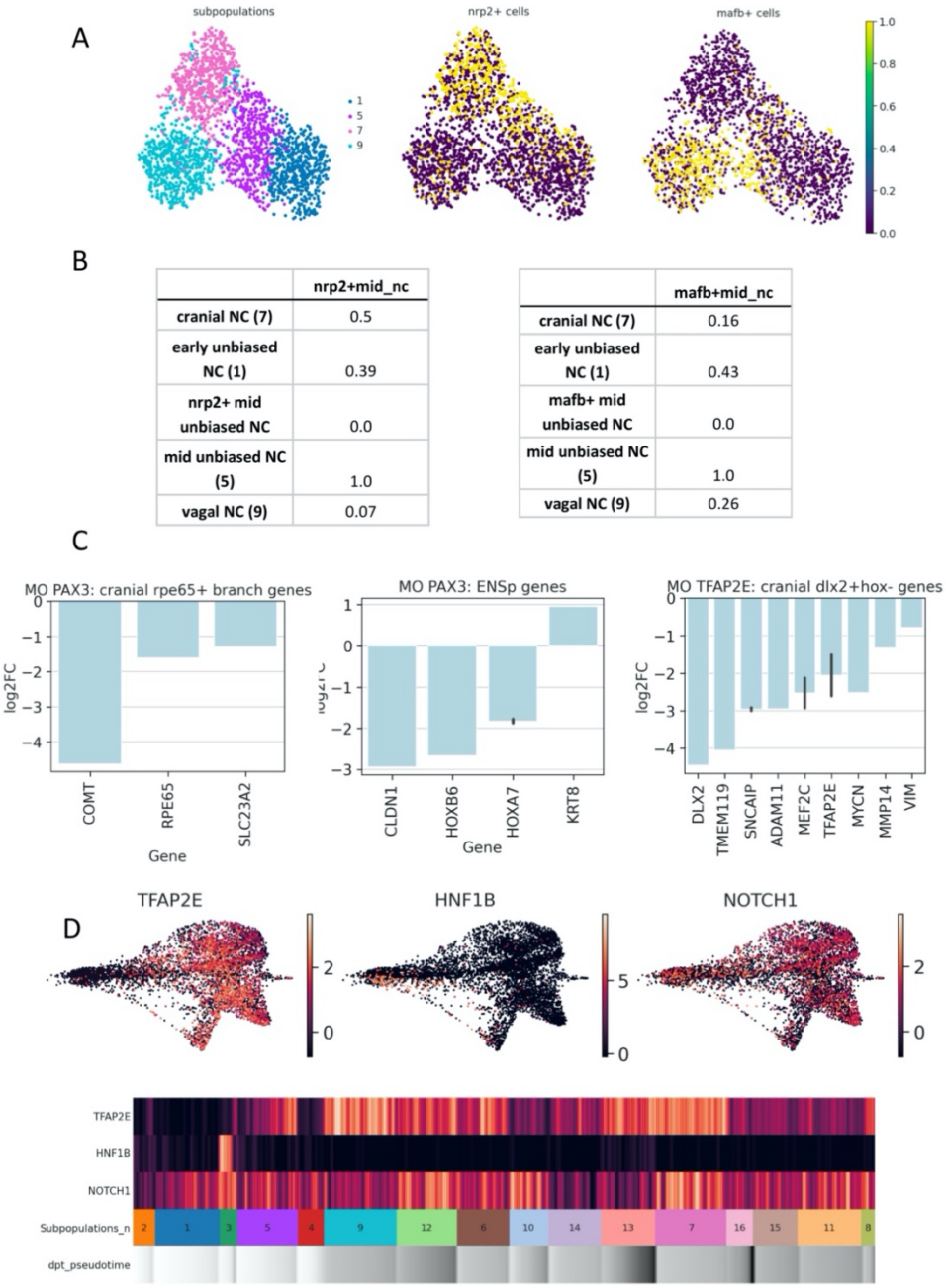

	nrp2+mid_nc
cranial NC (7)	0.5
early unbiased NC (1)	0.39
nrp2+ mid unbiased NC	0.0
mid unbiased NC (5)	1.0
vagal NC (9)	0.07

	mafb+mid_nc
cranial NC (7)	0.16
early unbiased NC (1)	0.43
mafb+ mid unbiased NC	0.0
mid unbiased NC (5)	1.0
vagal NC (9)	0.26

Fig. S9. In-depth cluster analysis. (A-B) *Mafb* and *nrp2* expression during cell cranial and vagal predisposition. **(A)** We find early minor predisposition within cluster 5 for of *mafb* or *nrp2* expression. Cells expressing *nrp2/mafb* above 80 percentile were sub-selected around the bifurcation: clusters 1, 5, 7, 9. PAGA revealed that *nrp2*$^{+}$ cluster 5 cells are 7 times more similar to the cranial state than to the vagal stage, and *mafb*$^{+}$ cells of unbiased cluster 5 are 1.5 times closer to the vagal state than to the cranial. **(B)** Tables with cluster-cluster similarities (calculated with PAGA). **(C-D)** Pax3 and Tfap2e direct roles during bifurcations in cranial and vagal NC. **(C)** Using Pax3 and Tfap2e depletion, we evaluated the change of expression of the late genes in the Pax3 and Tfap2e related branches. **(D)** Some Tfap2e targets confirmed with ChIP-seq and MO were not predicted by GRNboost2. For example, *hnf1b* with a very different expression pattern and *notch1* with a closely related expression pattern.

Table S1. Current scRNAseq datasets.
We analyzed current datasets of NC cells and compared it to our new dataset with the largest number of NC cells. This allows us to use complex ML approaches to reveal gene-gene relationships.

Dataset	NC selection	Cell number	Depth	Timing	scRNA-seq technology	Reference
GSE113074	X.tropicalis WE/markers	130000+ WE, 4700 NC	Low	9 gastrula and neurula batches	Indrops v2/v3	Briggs et al, 2019
GSE112294	Zebrafish WE/markers	63520 WE, 1770 NC	Low	7 gastrula & neurula batches	Indrops v1	Wagner et al, 2018
GSE106676	Zebrafish, foxd3+ cells	96 NC	High		SmartSeq2	Lukoseviciute et al, 2018
GSE130500 GSE131688	Chick, foxd3+	137 SmarSeq2 3000 10x	High + Low	Late neurula	SmartSeq2 10x	Williams et al, 2019
GSE129114	Mouse, wnt1/sox10+	200 NC	High	Neurula	SmartSeq2	Soldatov et al, 2019
GSE162044	Mouse, wnt1+ NC	1741 NC	High	Neurula	Smart-Seq2	Zalc et al, 2021
-	X.tropicalis WE/markers	140000+ WE, 6135 NC 17138 EC	Low	7 gastrula and neurula batches	Indrop v3	This study

Table S2. **Top NC specific genes for each developmental stage.**
Using Leiden clustering and differential expression analysis we constructed two datasets: Ectoderm and NC. Table represents the most specific genes expressed in the clusters in comparison to other cells of the whole embryo.

Cell type	NF stage	Cells number	Gene markers for cluster characterisation
EC	11	9190	SOX2, OLFM4. FOXI1, GATA2, SOX11
EC	12	3500	TFAP2C, C3, GATA2, OLFM4, ZEB2
EC	13	4448	TFAP2C, SOX9, OLFM4, LHX2
NC	12	623	C3, SOX9, ZIC1, SNAI2
NC	13	579	SOX9, SNAI2, C3, ZIC1
NC	14	416	SNAI2, TFAP2B, SOX9, SOX8
NC	16	882	TFAP2B, C9, C3, SOX10
NC	18	607	TFAP2B, C9, SOX8
NC	20	839	TFAP2B, SOX8, C9
NC	22	2253	TFAP2B, C3, C9, SOX10, DLX2

Table S3, S4, S5. **Top decreased genes in pax3 and tfap2e MO.**
Top decreased genes in Pax3 (left), Zic1 (middle), and Tfap2e MO (right) samples with the absolute expression change > 1000.

Gene_name	log2FC	abs_diff
oxnad1.l	-4.471306	2796.0
pou4f1.2.l	-3.792479	1208.5
stxbp5-like.1.l	-3.573356	1134.0
loc100498469-like.l	-3.269686	1227.5
slc12a2.l	-3.269554	1988.0
gatm.l	-3.219859	11768.5
pnhd.s	-3.189243	1104.5
sox9.s	-3.160360	3605.0
hnf1b.l	-3.122515	3153.0
pygm.s	-2.895865	2087.5
olig4.l	-2.869639	1287.0
loc733561.l	-2.836421	1099.5
msx1.l	-2.815328	5604.0
hoxb1.s	-2.729814	1538.0
hnf1b.s	-2.690841	2215.5
h1foo.s	-2.681030	1277.5
hyou1.l	-2.640135	1544.0
hoxd1.l	-2.637859	1410.5
hoxd1.s	-2.594724	2475.0
msx2.l	-2.587375	3742.5
olfm4.l	-2.565518	5451.0
pnp.l	-2.480788	2625.5
dhrs3.l	-2.469848	2506.0
ppat.l	-2.468018	2416.0
vim.l	-2.450922	4834.0
prkaa1.l	-2.350497	1045.5
snrnp70.l	-2.320323	11492.0
cdx2.l	-2.289480	2395.5
sp5l.l	-2.267839	3598.5
msx1.s	-2.267784	2652.0

Gene_name	log2FC	abs_diff
pappa2.l	-8.049168	1055.5
oxnad1.l	-5.325875	2855.0
loc733561.l	-4.275842	1212.5
crx.l	-4.005001	1355.0
h1foo.s	-3.891248	1411.5
crx.s	-3.755836	1057.0
cldn6.2.s	-3.040364	3454.5
nphp3.l	-2.975995	1040.5
xetrov90006074m.l	-2.862766	2312.0
pygm.s	-2.836971	2074.0
angpt4.s	-2.716769	1243.0
bnip3.l	-2.473468	1418.5
loc100498469-like.l	-2.436440	1116.5
slc12a2.l	-2.376951	1791.0
clpx.s	-2.376474	2285.0
cnn1.s	-2.336621	6767.5
pnp.l	-2.320125	2558.0
loc100495392.s	-2.270703	1480.5
cldn6.1.s	-2.254050	1493.0
pfkfb3.s	-2.213230	1744.0
mycl.l	-2.203118	2512.5
cyp26a1.s	-2.166806	1616.0
hoxc5.s	-2.105209	2095.5
abl1-like.s	-2.099759	1061.5
gad1.2.l	-2.075370	10114.5
rrm2.1.l	-2.036311	1825.5
tmod3.l	-2.035264	1362.0
s1pr5.s	-2.010914	1297.0
pds5a.l	-2.006197	2190.5
tiam1.s	-1.998983	2126.5

Gene_name	log2FC	abs_diff
sox10.s	-4.446147	6291.5
sox10.l	-3.973992	7541.0
sox8.s	-3.623336	2485.5
loc101735110.l	-3.294872	3226.0
loc100498368-like.s	-3.288774	6777.0
tp63.l	-3.282590	1379.5
fam212a.s	-3.190155	1215.0
fam212a.l	-3.189506	2014.5
tfap2b.s	-3.111449	2319.5
loc100498368-like.l	-3.058974	2636.5
foxd3.l	-2.979076	2062.0
adam11.l	-2.943961	1329.0
sox8.l	-2.803670	9715.0
endod1.l	-2.742037	1212.0
mafb.s	-2.642183	1447.0
kal1.l	-2.578369	1817.5
tfap2b.l	-2.529612	2642.5
mycn.s	-2.511291	1086.0
twist1.l	-2.453900	2819.5
twist1.s	-2.421903	2770.0
loc100124848-like.l	-2.401117	8166.0
fn1.s	-2.305269	4979.5
kiaa1217-like.l	-2.296111	1036.5
ahnak-like.s	-2.267407	3456.0
itln1.l	-2.252100	6428.5
lima1.l	-2.242827	2533.0
loc100497845-like.l	-2.208089	1035.5
itpr3.s	-2.194760	2438.5
aim1-like.1.s	-2.168639	1307.5
cmahp.l	-2.151611	1425.5

Table S6. **Pax3 ChIP-seq targets.**
Top MACS2 scored direct targets of Pax3.

chr	start	end	score	gene
chr8L	99475396	99475464	580	ASTL3A.1
chr9_10L	349156	349253	518	ATP6V0A1
chr7L	92931087	92931289	487	HES3
Scaffold46	813190	813276	484	ASS1
chr2L	176448007	176448188	448	PRCP
chr8L	118795321	118795461	440	FLAD1
chr8L	118785517	118785631	440	PSMD4
chr7L	89910794	89910942	435	VPS13D
chr3L	130428472	130431136	417	S1PR2
chr7L	15405111	15405195	390	INPP5A.1
chr6L	86407631	86407987	374	LYRM4
chr8L	119048876	119048973	368	EFNA3
chr1L	144729397	144731409	358	TBX3
chr5S	17252239	17252405	341	ATF3
chr4L	141138945	141139207	341	ATXN7
chr6L	37364463	37364585	314	HDAC9
chr6L	124571856	124571969	312	ZFAND1
chr6L	124583418	124583619	312	CHMP4C
chr4S	38950018	38950121	307	NAE1
chr9_10L	65487732	65488499	291	SLC25A12
chr5L	51178347	51178965	288	PSEN2
chr1S	115523395	115523481	286	NRL
chr6L	39747334	39747730	286	EVX1
chr9_10L	30759439	30759550	279	TGM3L.4
chr2L	88024978	88025202	267	HPCA
chr6L	82762756	82762905	266	CDH20
chr1S	12094861	12094998	263	FGFR3
chr8S	33705393	33705520	248	FUBP3
chr8L	57452010	57452126	245	SELENOW1
chr9_10S	23803020	23803090	244	USP36

Table S7. **Tfap2e ChIP-seq targets.**
Top MACS2 scored direct targets of Tfap2e.

chr	start	end	score	gene
Chr7	2771023	2771259	1502	RBM20
Chr4	136928957	136929250	1360	PIM1
Chr10	10458652	10458795	1353	ARL5B
Chr10	10464454	10464497	1353	PLXDC1
Chr5	13534757	13535087	1326	PTPN14
Chr10	50539112	50539288	1235	ARPC1A
Chr10	50529349	50529522	1235	PRKAR1A
Chr10	15734843	15734962	1218	SMARCD2
Chr2	2687034	2687603	1212	BOC
Chr9	85342807	85342887	1199	TNS1
Chr6	90349120	90349399	1198	TFAP2A
Chr6	47572683	47572824	1180	RARB
Chr4	58757061	58757134	1176	ANKRD11
Chr4	48790141	48791762	1170	BCAR1
Chr7	18235059	18235409	1164	JMJD1C
Chr2	138639744	138639788	1159	RBMS2
Chr8	6618399	6618453	1159	NOTCH1
Chr8	142072529	142072579	1153	CCT3
Chr8	142086526	142086803	1153	GLMP
Chr2	40958194	40958575	1153	PDK3
Chr1	65662851	65663810	1145	SPRY1
Chr4	67913743	67913832	1139	KCTD15
Chr9	83910392	83910819	1130	TUBA4A
Chr1	206833365	206833506	1100	RNF165
Chr1	16309482	16311265	1095	DCTN1
Chr1	16305342	16305426	1095	ADAM19
Chr10	11004405	11005055	1091	ARHGAP23
Chr6	12882851	12882961	1084	DHX30
Chr6	12892165	12892295	1084	LIMA1
Chr4	35478920	35479123	1071	PPP1R14B

Table S8. **Tfap2a ChIP-seq targets.**
Top MACS2 scored direct targets of Tfap2a.

chr	start	end	score	gene
chr8L	118798860	118799049	476	FLAD1
chr8L	118788167	118788453	476	PSMD4
chr5L	101986969	101987669	431	MCF2L.2
chr4L	74333641	74333831	423	ROR1
chr3S	83043144	83043215	395	LRIG3
chr4L	119344147	119344785	369	GPX1
chr9_10S	95234068	95234536	364	ARHGAP17
chr2L	110483824	110487409	352	SOWAHC
chr5S	1791004	1791317	341	SERTAD2
chr2L	91858061	91858536	329	MMP28
chr2L	91863324	91863411	329	TAF15
chr5S	83018695	83019717	323	PTMA
chr1S	179165531	179165761	318	CNTFR
chr1L	151166104	151166250	316	RPLP0
chr2S	158792498	158793672	316	LRTOMT
chr1L	151152633	151153237	316	GCN1
chr3L	136390271	136390378	307	ESR-5
chr4S	13935547	13940398	303	CHRM4
chr9_10L	109917922	109918127	303	LMF1
chr4S	13930436	13930514	303	MDK
chr4S	20597644	20598583	301	NAV2
chr1S	68374163	68374214	296	BTC
chr1S	56378070	56378168	295	EGF
chr1S	54034891	54035850	293	SPRY1
chr3L	28766498	28766650	275	MAT2B
chr8S	26253740	26253836	271	VGLL4L
chr9_10L	79461487	79461535	270	CDK15
chr9_10S	45513533	45514078	268	TNS1
chr7S	25366517	25366699	268	CPN1

chr3L	125880572	125880653	265	NOTCH3

Table S9. **Primers used in this study.**

primer name	purpose	sequence	reference
Snail2 Fwd pair1	ChIP-seq IP quality check	CCATCCCAACACCTGTCGTA	This study
Snail2 Rev pair1	ChIP-seq IP quality check	GCCCACCAGTTCACGTTCAT	This study
Snail2 Fwd pair2	ChIP-seq IP quality check	GCAATGCCTCAGCCTGTGAA	This study
Snail2 Rev pair2	ChIP-seq IP quality check	CAGCGCGTACTGCAATTCATTC	This study
Odc Fwd	qRT-PCR	GCCCTTTCTCCCTTTAACGC	(29)
Odc Rev	qRT-PCR	TGGTCCCAAGGCTAAAGTTG	(29)
Snail2 Fwd	qRT-PCR	CACACGTTACCCTGCGTATG	(77)
Snail2 Rev	qRT-PCR	TCTGTCTGCGAATGCTCTGT	(77)
Sox10 Fwd	qRT-PCR	CTATTACTGACACACGACGGAGC	(17)
Sox10 Rev	qRT-PCR	ACCTCTCATCCTCTGAATCCTGC	(17)
MyoD Fwd	qRT-PCR	TACACTGACAGCCCCAATGA	(29)
MyoD Rev	qRT-PCR	TGCAGAGGAGAACAGGGACT	(29)
Myl1 Fwd	qRT-PCR	GAAACACTTGGGCTGCTTTCTT	This study
Myl1 Rev	qRT-PCR	AGCAGGTTTAGCCTCAGGTTT	This study